Early stage diapirism in the Red Sea deep-water evaporites: origins and length-scales

DOI:
10.1016/j.tecto.2022.229331

Early stage diapirism in the Red Sea deep-water evaporites: origins and length-scales

Neil C. Mitchell[1]*, Karina Hernandez[2], Jonas Preine[3], Marco Ligi[4], Nico Augustin[5], Ay Izzeldin[6], Christian Hübscher[3]

[1]Department of Earth and Environmental Sciences, University of Manchester, Williamson Building, Oxford Road, Manchester M13 9PL, U.K.

[2]Instituto Mexicano del Petróleo, Ciudad de México, México

[3]Universität Hamburg, Mittelweg 177, 20148 Hamburg, Germany

[4]Istitutodi Scienze Marine, CNR, Via Gobetti 101, 40129 Bologna, Italy

[5]GEOMAR, Dienstgebäude Ostufer / East Shore Building Wischhofstr. 1-3, D-24148 Kiel, Germany

[6]Awasconrc, Gereif W, H4, Bld 376, Khartoum, POB 410, Khartoum, Sudan

*Corresponding author.

Keywords: salt tectonics, salt diapirism, halokinetics, variogram

This is the green open-access version of the above article accepted for publication in the Elsevier journal Tectonophysics 1 April 2022 (doi:10.1016/j.tecto.2022.229331).

Abstract

Rayleigh-Taylor models for diapirism predict that diapirs should develop with characteristic spacings, whereas other models predict varied spacings. The deep-water Miocene evaporites in the Red Sea provide a useful opportunity to quantify length scales of diapirism to compare with model predictions. We first review the stratigraphy of the uppermost evaporites in high-resolution seismic data, revealing tectonic growth stratigraphy indicating that halokinetic movements occurred while the evaporites were being deposited. In some places, movements continued after the Miocene evaporite phase. The S-reflection marking the top of the evaporites is an erosional surface, in places, truncating anticlines of layered evaporites. In others, reflections within the uppermost evaporites are conformable, suggesting a lack of erosion. The top of the evaporites therefore had relief at the end of the Miocene. We select for numerical analysis 14 long profiles of topography of the S-reflection. Variograms derived from them after detrending reveal minor periodicity, though with varied wavelength, and varied roughness of the surface. However, an average variogram computed from these profiles is nearly exponential, indicating that the evaporite surface is mostly stochastic with no uniform scale of diapirism. An exponential model fitted to that average variogram suggests a spatial range over which the S-reflection topography becomes decorrelated of 3 km, which is comparable with the mean vertical thickness of the evaporite body. Power spectra of the evaporite surface are flatter at long wavelengths, which we interpret as due to weakness of halite preventing large surface relief from developing. The results suggest only modest periodicity, so the Rayleigh-Taylor model does not explain deformation in the Red Sea evaporites studied here. Their topography may turn out to be useful for suggesting the vertical scales and lengthscales of relief to expect of early stages of other salt giants, such as that of the Santo Basin.

1. Introduction

Salt diapirism is a fundamental geological process that has influenced the structures of many passive margins around the Earth including the "salt giants" of the Atlantic Ocean and Gulf of Mexico (Bonatti et al., 1970; Evans, 1978; Pautot et al., 1970; Rona, 1982). The associated structures make them of interest for hydrocarbon exploration and potentially for nuclear waste and CO_2 storage. Given the unique deformation style of salt (evaporitic sediments), its widespread occurrence and influence on stratigraphic development of many passive margins, the analysis of salt diapirism is an important component of the analysis of sedimentary basins. However, evidence documenting the early salt movements, which is needed for understanding the dynamics of the salt, is typically obscured because the halite component of salt deposits is commonly strongly mobilised, complicating the stratigraphy (Hudec and Jackson, 2006). Early models of salt diapirism involved an assumption that density differences between the salt and overlying deposits caused Rayleigh-Taylor instabilities to develop (Berner et al., 1972; Biot and Odé, 1965; Nettleton, 1934). In such models, layered geological structures are treated as fluids with differing density, and the models predicted that diapirs should grow with a characteristic wavelength that depends on the layer thicknesses and viscosities (Fernandez and Kaus, 2015; Hughes and Davison, 1993; Turcotte and Schubert, 1982). However, subsequent studies of salt deposits have found more complex relationships and generally a lack of a single wavelength of salt-structures, thus challenging the applicability of Rayleigh-Taylor models. For example, Hernandez et al. (2018) found that ratios of diapir wavelength to layer thickness for diapirs from the Southern North Sea varied in ways not explained by Rayleigh-Taylor models, but may be explained by changes in wavelength with progressive diapirism. Furthermore, if the overlying layer has a plastic rheology, more complex diapirism can be expected (Poliakov et al., 1993). Analytical modelling by Ismail-Zadeh et al. (2002) involving a plastic overburden suggested that diapirism may occur with a wide range of wavelengths.

Hernandez (2020) analysed the topography of the top surfaces of evaporite (salt) bodies from the Levant (Gvirtzman et al., 2013), Kwanza (Hudec and Jackson, 2011), Santos (Pichel et al., 2017) and North Sea Zechstein (Harding and Huuse, 2015) basins using spectral methods. She found that they lacked clear spectral peaks that would be expected of Rayleigh-Taylor diapirism and instead declining spectral power over length scales 0.1 to 70 km. Hernandez (2020) suggested that the varied salt-structure spacings of those deposits could originate from a number of causes depending on location, including varied loading by overlying strata, varied density and viscosity of the evaporites, heating by intruding dykes, underlying fault escarpments promoting diapirism, regional tectonic shortening and the plastic deformation mentioned earlier. Effects on diapirism of underlying basement structure, particularly faults, are also explored by Harding and Huuse (2015).

To improve understanding of the factors leading to the geometries of evaporite deposits, examples are needed with fewer of the complicating factors identified by Hernandez (2020), in particular, deposits with low-density overburden. The Levant Messinian evaporites, for example, have present overburdens of ~500 m or more, and seismic data reveal that deformation started while the evaporites were being deposited (Gvirtzman et al., 2013; Hübscher and Netzeband, 2007; Netzeband et al., 2006; Reiche et al., 2014). Lithospheric loading by the Levant evaporites and other sediments caused regional tilting, which led the evaporites to creep down-gradient, creating internal folding and thrusting (Hübscher and Netzeband, 2007).

The Red Sea provides another structurally simple example of shallowly buried evaporites of much younger age (Miocene) than the evaporites of the Atlantic and Gulf of Mexico margins. The few published seismic reflection datasets imaging the evaporites internally reveal alternating patches of transparent and layered reflectivity likely due to halite-dominated diapirs and strata containing more diverse lithologies, respectively (Colombo et al., 2014; Izzeldin, 1987; Izzeldin, 1989; Ligi et al., 2019a; Rowan, 2014). Those alternations are similar in character to seismic data of many parts of the Aptian evaporites of the Santos Basin (Davison, 2007; Davison et al., 2012; Fiduk and Rowan, 2012; Guerra and Underhill, 2012; Jackson et al., 2015a; Mann and Rigg, 2012; Maul et al., 2021; Mohriak et al., 2012), so the Red Sea may turn out to be analogous. Lithological logs from six wells in the Santos Basin (Jackson et al., 2015b; Jackson et al., 2014) show it to be halite-dominated, but with varied amounts of anhydrite, carnallite and carbonate. Alternatively, some seismic records from the Santos Basin have been interpreted as showing evaporites comprising two cycles each of halite-dominated strata overlain by more strongly seismically reflective evaporites containing anhydrite (Fiduk and Rowan, 2012). Although the stratigraphy in the Santos Basin is somewhat different from the Red Sea evaporites, which are halite-dominated in their lower parts overlain by layered evaporites containing anhydrite and shale (described later), in both basins the stratigraphy implies layered rather than homogeneous physical properties.

The presence of anhydrite potentially complicates interpretation or modelling of evaporite movements (salt tectonics) because its density is one third larger than that of halite and it is likely to be stronger, although its rheology under *in situ* conditions is poorly known (Urai et al., 2017). If the evaporites of the Red Sea are flowing at rates comparable to half the Nubia-Arabia plate separation rate (Mitchell et al., 2021) and flowage occurs over 100-1000 m vertical thickness, we estimate average strain rates of order 10^{-13}-10^{-12} s^{-1}. Extrapolation by Dorner et al. (2014) of their results of creep measurements on dry anhydrite to such strain rates suggests that temperatures of a few hundred degrees would be needed for anhydrite to deform by dislocation creep. Such temperatures are much higher than 100-200˚C expected for the upper kilometre of the evaporites from modelling of surface heat flow data (Makris et al., 1991; Martinez and Cochran, 1989). At faster strain rates (10^{-5} s^{-1}), experiments by Hangx et al. (2010) led to cataclastic failure. These results leave open the question of how trace water, which strongly affects halite rheology (Urai et al., 1986), would affect anhydrite rheology, although a non-uniform rheology is also suggested by anhydrite-rich layers commonly broken up into segments called "stringers" amongst halite (Rowan et al., 2019). Nevertheless, Rowan et al. (2019) suggested that the varied presence of non-halite rocks can be modelled with an effective viscosity varying by five orders of magnitude. Analysis of folded rock salts suggests effective viscosity contrasts with halite of X10-100 where layers included anhydrite showing evidence of solution-precipitation creep (Schmalholz and Urai, 2014) and X10-20 in halite with alternating layers with varied impurities (Adamuszek et al., 2021). Therefore, the Santos and Red Sea evaporites likely have both had strong internal rheological and density variations since their deposition. As we explain below, the Red Sea evaporites have been migrating towards the rift centre as a result of differential subsidence, also like those of the Santos Basin (Davison et al., 2012; Fiduk and Rowan, 2012; Jackson et al., 2015a; Quirk et al., 2012; Warsitzka et al., 2021). For this variety of reasons, the Red Sea evaporites may turn out useful as an analogue of those of older basins, potentially suggesting the relief of those their early-stage evaporites. In turn, the processes inferred for those older basins may also apply to the Red Sea evaporites, where high-quality deep seismic reflection data are not publicly available.

Despite the lack of publicly available digital deep seismic data in the Red Sea, studying the geometry of the evaporite surface is straightforward because, in shallow seismic data, it is marked by a prominent reflection ("S-reflection"), which appears throughout most of the basin (Knott et al., 1966; Phillips and Ross, 1970; Ross and Schlee, 1973). As those data have high resolution and the evaporites are shallower, they also allow a more detailed examination of the nature of the top of the evaporites than is often the case with data from the other basins. Furthermore, in contrast with the Levant evaporites, those in the deep waters of the Red Sea away from coasts are generally buried by only 200-300 m of low-density Plio-Pleistocene hemipelagic deposits and the overall environment is extensional, not compressional (Mitchell et al., 2010; Mitchell et al., 2017). It therefore provides a useful basis to study evaporite body diapirism without a density inversion with overlying sediments and in an extensional regime that is somewhat analogous to the earlier Santos Basin. In this study, our objectives are to (i) review the stratigraphy of the uppermost evaporites in high-resolution seismic data to improve understanding of halokinetic movements during and after the evaporite deposition, (ii) calculate variograms to characterise stochastic and cyclic components of the evaporite surface topography and (iii) use power spectra to investigate whether of the evaporite surface has periodic components.

2. Background to the Red Sea evaporites

According to Hughes and Beydoun (1992), most of the evaporitic sediments in the Red Sea were deposited from about the start of the Miocene until the end of the Miocene. Halite-dominated evaporites were deposited in the Middle Miocene, followed, in the Upper Miocene, by layered evaporites containing abundant anhydrite. In the Egyptian stratigraphy, the latter are called the "Zeit Formation". Sediment samples from the uppermost evaporites were recovered in deep water by drilling during Deep Sea Drilling Project (DSDP) Leg 23B at the three sites marked in Figure 1. The stratigraphy of those samples is summarised in Figure 2, revealing the layered evaporites as containing alternating halite, anhydrite and shale at Sites 225 and 227, and anhydrite and shale at Site 228. Correlating that stratigraphy with seismic reflection data suggested that a prominent reflection seen throughout the Red Sea (the "S-reflection" (Ross and Schlee, 1973)) corresponds with the top of the Miocene evaporites or a layer of rigid shale immediately above it (Whitmarsh et al., 1974). Colombo et al. (2014) found that the S reflection corresponded with anhydrites at the top of the evaporites in a commercial well located in their area 1 marked in Figure 1.

Izzeldin (1987) described images of the evaporites in deep-seismic reflection data as showing either transparent or layered reflectivity, with the latter more common towards the top. The layered reflectivity likely corresponds with the layered stratigraphy found at the DSDP sites, whereas the transparent reflectivity probably corresponds with the massive halite (Hughes and Beydoun, 1992). Reflectivity varying from layered to more transparent has also been reported in other seismic datasets and reflections within it commonly appear to be folded (Colombo et al., 2014; Ehrhardt and Hübscher, 2015; Izzeldin, 1989; Ligi et al., 2018; Mitchell et al., 2019; Rowan, 2014). The seismic data shown in Colombo et al. (2014) suggest that transparent regions extend ~10 km laterally near the Arabian coast.

A topographic map of the S-reflection (Mitchell et al., 2017) was updated with a commercial 3D seismic dataset from the Egyptian Red Sea by Mitchell et al. (2019) and here with new sparker seismic data from the Sudanese Red Sea (Augustin et al., 2019). The result in Figure 1 reveals a number of influences, which are described by Mitchell et al. (2021). Along the coasts, some deep depressions of the S-reflection occur, such as marked in Figure 1, where the evaporites have been loaded by terrigenous sediments. Away from those areas, loading is by hemipelagic sediments of lower density than halite (Figure 3). From a reconstruction of the average surface elevation of the deep-water evaporites (Mitchell et al., 2021), they were likely deposited to ~200 m below modern sea-level at the Miocene-Pliocene boundary. They have subsequently subsided because of thermal cooling of the lithosphere, because of some halite dissolution and because of deflation associated with a general flowage of the evaporites towards the centre of rifting (located roughly by the deeps marked in Figure 1). That flowage has been non-uniform, being greatest where there are presently inter-trough zones of evaporites marked in Figure 1 covering the spreading axis. Near those areas, the evaporite surface typically has a lower elevation away from the rift axis, caused by a greater deflation of the evaporite surface compensating for greater flowage towards the axis. In contrast, the evaporites remain high where flowage is retarded by a basement of higher elevation, which in places blocks flowage (Mitchell and Augustin, 2017; Mitchell et al., 2010). Truncated reflections at the top of the evaporites (Colombo et al., 2014; Izzeldin, 1989) have been interpreted as evidence of erosion, either subaerially or by surface waves or both, and thus that the Red Sea likely drew down abruptly at around the Miocene-Pliocene boundary (Mitchell and Augustin, 2017; Mitchell et al., 2021).

3. Data and methods

3.1. Seismic reflection datasets

To illustrate a range of halokinetic and other structures, a selection of seismic reflection data is assembled in Figure 4 from survey lines located in Figure 5. The data in Figures 4a and 4b were collected on RV *Urania* during cruise RS05 (Ligi et al., 2012; Ligi et al., 2011; Mitchell et al., 2010) and involved a 48-channel short streamer with 12.5 m group interval with two Sercel GI-Guns as the source. These data have been processed in a manner that preserved amplitude ratios and the highest frequency contents to improve resolution of reflections within the evaporites and the S-reflection from the evaporite surface. After predictive deconvolution, a time-varying prestack bandpass filter was applied with tapering from 12 to 16 and from 96 to 120 Hz.

The data in Figures 4c-4e were collected on RV *Robert Conrad* during cruise RC0911 with a 25-cubic inch airgun source and short streamer. Recording was onto paper, but, despite their age (collection in 1965) and the analogue technology used, the data are of good quality.

The data in Figure 4f were collected on RV *Pelagia* during cruise 64PE-445 as part of the SALTAX project (Augustin et al., 2019). As a seismic source, a Delta Sparker system with a dominant frequency of ~300 Hz was used. Seismic energy was recorded using a Microeel solid-state streamer with 24 channels and a length of 100 m. Data processing was carried out using VISTA software and comprised trace-editing, simple frequency filtering (50 – 2000 Hz), normal moveout correction (1500 m/s), common mid-point stacking, finite-difference post-stack migration, as well as top-muting and white noise removal. Interpretation of the seismic data was carried out using the KingdomSuite software of IHS.

Figure 4g shows the westerly side of line 19 of Izzeldin (1987). These data were collected with a Vaporchoc source and a streamer of 2.4 km length. Move-out corrections were applied but not migration. These data were available only in analogue form.

3.2. Power spectral analysis

Power spectra of topography are useful to determine whether cyclical components exist, as they should produce spectral peaks. Alternatively, many topographic datasets show inverse power relationships between power spectral density and wavenumber (Bell, 1975; Fox and Hayes, 1985; Gilbert and Malinverno, 1988; Rapp, 1989). In some of those cases, the topography may be self-affine fractal (Gilbert and Malinverno, 1988; Turcotte, 1991), implying a lack of dominant wavelengths.

For assessment of cyclicity and stochastic character, long data series are preferred in order to capture multiple wavelengths. However, the large-scale morphology of the evaporite surface in Figure 1 shows many areas where the surface is depressed over 10s to 100 km scales by processes other than the diapirism studied here. For example, a large collapse structure lies northeast of the two DSDP sites (225 and 227). Large depressions of the S-reflection occur near to the coasts due to the terrigenous sediment loading. Furthermore, salt walls tend to be oriented parallel to the coasts (Mitchell and Augustin, 2017), so lines perpendicular to them should be preferred to capture any preferred spacing or wavelength (Hernandez et al., 2018). Based on these considerations, the data between the red circles in Figure 6 were selected for cyclical analysis. These data are mostly from the same seismic reflection dataset (Izzeldin, 1982) and hence are of a common quality. They cross the Red Sea almost perpendicularly. Segments of data were chosen to avoid the steep slopes into the deeps or spreading axis (grey highlighted in Figure 6) as well as the large deflated areas adjacent to inter-trough zones.

Those data segments (14 in total) were detrended by fitting a least-squares regression line to each profile and storing the regression residuals as data series for the following analyses. An example segment of detrended data is shown in Figure 7. Those detrended data were prepared for power spectral analysis following the same procedure as Hernandez (2020) to allow later comparison with her results. To prevent spectral leakage where the ends of each detrended series were unequal (Percival and Walden, 1993), this preparation involved multiplying by a Kaiser window and interpolating to ensure cyclicity. Following Turcotte (1997), the cyclical components of the treated data series were found by computing Fourier transforms using the Cooley and Turkey (1965) method implemented in Matlab™. Power spectral densities were computed from the amplitudes of those components.

3.3. Variogram analysis

Variograms can be used to characterise stochastic and cyclic components of data series (Davis, 2002; Matheron, 1963). They have been derived for natural topographic datasets, e.g., for seabed classification (Herzfeld, 1993; Herzfeld et al., 1995; Herzfeld and Overbeck, 1999) and to characterize sedimentary bedforms (Robert and Richards, 1988; van Dijk et al., 2008). The empirical semi-variogram is estimated from a regularly sampled data series y_i (Matheron, 1963):

$$\gamma_h = \frac{1}{2(n-h)} \sum_{i=1}^{n-h} (y_i - y_{i+h})^2 \qquad (1)$$

where y_{i+h} is a lagged version of the data series y_i, n is the number of samples in the series and h is the number of samples corresponding with the lag distance. (In the following, we refer to γ_h as the variogram, omitting the "semi" for brevity.) Implementing the calculation in equation (1) involves moving a copy of the data series a lag h number of cells, taking the difference of the lagged and original versions where they overlap each other, and summing the squares of those differences. Where the two series are strongly correlated, the difference leads to small γ_h. Conversely where they become uncorrelated, γ_h increases. A pure sinusoidal data series results in γ_h that is almost sinusoidal also, oscillating from zero to a maximum value, representing lags where the two series are uncorrelated or correlated, respectively. For more typical stochastic topography, γ_h tends to rise towards a maximum value (the "sill") that equals half the variance of the topography. The distance over which it does so (the "range") represents a typical length scale of the variations. Variograms were derived here using equation (1) from the same data series used for the power-spectral analysis, i.e., the 14 segments between the red dots in Figure 6 after detrending as explained earlier.

4. Results

We refer to the S-reflection below simply as "S" for brevity. In this section, we first study the nature of S and stratigraphy around it in the seismic reflection data to assess what the topography of S is likely to represent, in particular, whether it reveals vertical differential displacements since 5.3 Ma, the end of the Miocene.

4.1. Observations

In the RV *Conrad* data, S tends to be sharp where the underlying layering (within the evaporites) conforms with it, such as in Figures 4c-4e where marked "layered evaporites." Away from those areas, S can be more diffuse as marked in those figure panels. A similar association between sharp S and layered evaporites (and diffuse S where layered evaporites are visually absent) can be observed in the sparker seismic data in Figure 4f.

Where the evaporites are reflective, individual reflections can, in places, diverge with each other and with the S-reflection, typically increasing in dip with depth. Examples are marked "tectonic growth stratigraphy" in Figures 4a, 4b and 4c. In contrast, in the limited segments of layered reflectivity in Figures 4c-4e, reflections do not appear to vary in dip with depth. Some nearly horizontal reflections beneath S can be observed immediately SE of the "anticline in Figure 4a, within the syncline in Figure 4b and where S is marked in just left of centre in Figure 4c. However, the majority of the reflections within the evaporites in Figure 4 are dipping, not flat. In many places, they are curved, either upwards or downwards, in places sharply (e.g., under westerly "P" in Figure 4d).

Figure 4a reveals that reflections within the evaporites abruptly terminate at S where marked "erosional surface". A similar truncation of evaporite reflections occurs locally above the anticline marked. In Figure 4b, reflections to the SW of the syncline terminate at S. Where those reflections terminate, S has fine-scale relief that has created diffraction hyperbolae in the section. Similar truncations of evaporite reflections at S can be observed in seismic data from other parts of the Red Sea (Bonatti et al., 1984; Feldens et al., 2016; Guennoc et al., 1988; Izzeldin, 1987; Knott et al., 1966; Mitchell et al., 2017; Mitchell et al., 2021; Ross and Schlee, 1973). Figure 8 summarises occurrences of such truncations interpreted from seismic data from the central Red Sea. (Due to varied data quality and coverage, absence of these observations is not evidence of their absence, rather the map is intended to show how common they are.)

In contrast, in areas marked "layered evaporites" in Figures 4c-4f, reflections beneath S are conformable with it and do not appear to be truncated. Other examples of conformable reflections can be observed in other published seismic reflection data (Bonatti et al., 1984; Cochran, 2005; Ehrhardt and Hübscher, 2015; Ligi et al., 2018; Ligi et al., 2019a; Mitchell et al., 2017; Phillips and Ross, 1970; Richter et al., 1991; Rowan, 2018).

There is some variation in thickness and character of the Plio-Pleistocene (PP) sediments overlying S. In Figure 4a under the area marked "Basin", reflections in the lower PP are roughly conformable with S, but reflections are more nearly horizontal (nonconformal) in the upper PP. Above the anticline in that panel, the stratigraphy is disrupted by small faults. In Figures 4c and 4d, the sediments overlying S appear mostly conformable with it. In Figure 4f, two similar segments of conformable reflections are marked "P". To the SW, however, the section shows PP sediments infilling the syncline.

4.2. Interpretations

The divergent reflections within the uppermost evaporites are evidence of tectonic growth stratigraphy and their presence indicates that halokinetic movements were occurring during evaporite deposition. The filled syncline in Figure 4f suggests that such movements in places continued into the PP, whereas in other places tectonic growth stratigraphy does not continue into the PP (e.g., Figures 4a and 4b), suggesting that locally vertical differential movements locally stopped by the Pliocene. Tectonic growth stratigraphy can be observed in published seismic reflection data showing the uppermost evaporites in many other parts of the deep-water Red Sea (Bonatti et al., 1984; Cochran and Karner, 2007; Colombo et al., 2014; Guennoc et al., 1990; Guennoc et al., 1988; Izzeldin, 1987; Ligi et al., 2019a; Mart and Ross, 1987; Richter et al., 1991; Rowan, 2014). The published seismic images showing growth stratigraphy stopping near the Miocene-Pliocene boundary include a line across Vema Deep near 24˚N (Bonatti et al., 1984, their figure 6b) and various line-drawings of seismic data from the southern Red Sea (Phillips and Ross, 1970; Ross and Schlee, 1973). Growth stratigraphy apparently continuing into the PP can be found in seismic reflection data near 27˚N (Cochran and Karner, 2007), 26˚N (Ligi et al., 2018; Ligi et al., 2019a; Richter et al., 1991) and 18˚N (Ross and Schlee, 1973), and in other seismic datasets (Phillips and Ross, 1970).

Ongoing, but heterogenous, deformation is also suggested by the varied presence of tectonic disruption of the PP (e.g., locally above the anticline in Figure 4a and in other data

(Mart and Ross, 1987; Uchupi and Ross, 1986)). The varied character of S could also be explained by varied deformation, if this reflection is diffuse where the top of the evaporites has been disrupted by small faults. Such disruptions were observed through much of the PP cored during DSDP Leg 23 (Stoffers and Kühn, 1974) (Figure 2) and are suggested by a fine-scale rugosity apparent in high-resolution multibeam sonar data of the PP sediments overlying evaporite flows (Feldens and Mitchell, 2015; Mitchell et al., 2010).

Erosion of the surface now forming S has been suggested to have occurred by wave erosion (Mitchell et al., 2017) or exposure to rainwater (Colombo et al., 2014), in either case associated with an abrupt short-lived drawdown of the Red Sea level at the end of the Miocene or in the earliest Pliocene (Mitchell et al., 2021). As some parts of S do not show erosional features, the evaporite surface may have not been perfectly flat at that time so that some parts of it remained submerged during the sea level drawdown. For example, in the SE half of Figure 4e, two segments of layered evaporites without erosional surfaces are separated by two hills of S with no internal reflections. If these hills are diapirs, they may have also had some positive relief at the end of Miocene, while the surrounding layered evaporites formed depressions. Those depressions were either protected from wave erosion by limited fetch caused by the diapirs forming islands, or the water level did not fully draw down so that the layered evaporites did not get exposed to rainwater. Although the mechanism is unclear from these data, S appears to have had varied experience of erosion or no/little erosion.

From these arguments, S was not perfectly flat at the end of the Miocene and therefore the topographic variation of S does not exactly represent differential vertical movements that have occurred since that time. Nevertheless, diapiric movements are progressive. While we observe evidence that some diapiric movements stopped after the

Miocene, we have not observed any evidence that they reversed. Consequently, the topography of S should represent the horizontal length scales of deformation, even if the inferred vertical displacements are only maxima.

4.3. Power spectra

The power spectra shown in Figure 9 for individual line segments are somewhat noisy and have local peaks but no common peak, suggesting a general lack of a dominant wavelength. A possible exception is a modest peak revealed in the averages of those spectra at $\log_{10}(1/\lambda)$ of -1.39 (λ=25 km), although it does not appear to arise from peaks in all segment spectra. The averages form an inverse power-law trend for $\log_{10}(1/\lambda) > -1.1$ (λ<13 km), with power spectral density varying by an order of magnitude between individual spectra. The regression line shown suggests PSD ~ $(1/\lambda)^{-3.05}$. For $\log_{10}(1/\lambda) < -1.1$ (λ>13 km), the average spectrum flattens besides the peak mentioned. This is a feature also seen in larger-scale topography (e.g., Gilbert and Malinverno, 1988).

If the evaporite topography were a self-affine fractal over the 1-13 km wavelength range, the fractal dimension would be $D=(5-\beta)/2$ (Turcotte, 1997) where β is the power-law exponent. (Such a geometry would be interesting here as fractals do not possess characteristic wavelengths, but rather a range of wavelengths (Turcotte, 1991).) The value D=0.98 computed from β=3.05 for the data in Figure 9 is somewhat lower than those of other topographic data, which tend to be closer to D=1.5 (Turcotte, 1991). It is slightly outside the range of permissible values of D which strictly speaking must be larger than unity for the geometry to be a fractal (Malinverno, 1989). It is close to values for D found for ocean floor bathymetry of abyssal hills (Gilbert and Malinverno, 1988). However, like abyssal hill terrains, which vary in underlying geology from exposed bedrock to sedimented basins and thus are not truly fractals (Herzfeld et al., 1995; Herzfeld and Overbeck, 1999), the seismic records in Figure 4 show a range of character of the evaporites at the S reflection. Furthermore, its topography (Figure 6) varies in character between and within different lines, unlike topographic simulations developed with *D*=1 (Malinverno, 1989). The evaporite surface therefore appears not to be a self-affine fractal, although, like fractals, it does contain hills and valleys with a range of lengthscales, not as expected if the Rayleigh-Taylor model applied.

The flattening of the average power-spectrum below $\log_{10}(1/\lambda) = -1$ could be a sign of internal evaporite isostatic effects. In that interpretation, processes that cause roughening of the evaporite surface over the 1-13 km range are not able to generate relief at the 13-100 km range because of the weakness of the halite component of the evaporites. We explore this further in the discussion.

4.4. Variograms

In the following, the variograms are referred to with shortened identifiers according to the data series that they were computed from, e.g., "Bannock1" refers to the variogram for Bannock line 1 and Iz7 to Izzeldin line 7. The variograms in Figure 10 generally rise towards a more stable level at a lag distance varying from only ~2-3 km for Iz15 to ~10 km for Bannock1. The level that they settle at (the variogram "sill") also varies greatly between lines. The sill is smallest for Iz17b (~2000 m^2) and largest for Bannock1 (~16000 m^2). As these represent half the data variance (Matheron, 1963), they imply that the standard deviation (σ=$\sqrt{}$variance) of the evaporite detrended topography varies from ~63 m to ~179 m.

Furthermore, individual variograms oscillate markedly differently. For example, that of Bannock1 has two peaks implying decorrelation occurred where the lag reached 5 and 12 km. In Figure 6, this appears to be due mainly to the salt structures around 2-4 km distance.

The variograms for Iz15, Iz9a, Iz17a, Iz21 and Iz19 also each have two peaks, implying the presence of at least two spatial frequencies (Robert and Richards, 1988). In contrast, the Iz17b variogram reaches a sill level with only minor oscillations, suggesting that the topography is mainly stochastic. That profile in Figure 6 also shows a lack of regular oscillations.

The blue line in Figure 10 is an average of the 14 variograms shown. Its initial rise from the origin to *h*=2 km is upwards-concave, rather than downwards-concave as would be expected from a nugget effect arising from random noise. This concave-upwards shape indicates that the topographic data are partly correlated over short length scales, mainly a result of the resolution of the data series. Continuing the gradient back to the horizontal axis suggests a resolution of <1 km. Besides this effect, the average has a simple form and is almost exponential. The red dashed line in Figure 10 represents the following function fitted by least-squares to the data (Robert and Richards, 1988):

$$\gamma(h) = c\left(1 - e^{-h/r}\right) \quad (2)$$

where *c* is half the data variance and *r* is an exponent. The sill of the average variogram in Figure 10 is 9428 m^2, implying σ=137 m. Parameter *r* representing the range of variability or distance over which topographic features decorrelate is 3.0 km. The average peaks at 8 km and declines slightly to 12 km lag, suggesting possibly some average periodic component, although the number of lines analysed is small, so its significance is unclear. If the average structure is cyclic, the peak at 8 km represents decorrelation where the copy of the data series has been translated by a lag of half a wavelength, so this would imply a full wavelength of that structure of ~16 km. In practice, the S-reflection topography in Figure 6 contains many spatial wavelengths, many of which are smaller than 16 km. The 8-km decorrelation scale however appears to be an upper limit of the distance between any individually adjacent peak and trough.

Equation (2) was also fitted to the individual variograms. The resulting values of σ vary from 72 to 181 m. Figure 11a shows that roughness σ tends to be larger in the north and to the west. The range *r* varies from 1.1 to 7.9 km (Figure 11b). The largest range was found on line Iz25, where it appears to be associated with a long-wavelength undulating structure (Figure 6). The shortest range was found on line Iz19.

5. Discussion

From the above analysis, the Red Sea Miocene evaporites have a stochastic surface lacking clear periodicity that would be expected of Rayleigh-Taylor models. Their rugosity is modest as expected of a pillow phase of diapirism. Here we explore explanations for these properties and how diapirism in the Red Sea compares with diapirism in some other basins.

5.1. To what extent does preserved topography of the S-reflection arise from a threshold differential stress for halite deformation?

Rowan et al. (2019) suggested that a differential stress of order 1 MPa is typically needed for halite to deform, hence some of the Red Sea evaporite relief generated by processes other than diapirism (e.g., faulting associated with widespread flowage) could be supported by rigidity of the evaporites. It is difficult to assess differential stress within the Red Sea evaporites accurately without numerical modelling, though stresses are likely to arise from their topography both at long wavelengths from gravitational loading associated with the gradient of the evaporites flowing into the axial region and at short wavelengths from local relief of the evaporite surface. The former is less important to the discussion here, though we note that gradients around the margins of the deeps reach 0.1 m/m and locally 0.2 m/m (Mitchell et al., 2010). From equation 4a of Mello and Pratson (1999), these gradients imply that differential stresses pass the threshold 1 MPa by 100 m depth below the evaporite surface if unsedimented and shallower if they are further loaded by Plio-Pleistocene sediments.

Evaluating the short-wavelength sources of differential stresses is more complicated as the evaporites are variably extending, folding and undergoing strike-slip movements due to flowage (Mitchell et al., 2010) and the surface variations have a range of scales and gradients. However, a 100 m difference in level of halite displacing water would lead to a difference in static vertical stress of 1.15 MPa. Hence, some small-scale topography is likely supported by the halite, potentially explaining how small faults at the seabed remain observable in multibeam sonar data (Augustin et al., 2014; Augustin et al., 2016; Mitchell et al., 2010). In contrast, the larger-scale topography is more likely to lead to stresses above 1 MPa if not compensated isostatically by internal density variations as discussed in the next section.

Some seismic sections of the Santos Basin evaporites also show fine-scale topographic relief (Davison, 2007; Fiduk and Rowan, 2012; Mann and Rigg, 2012; Mohriak et al., 2012). Unfortunately, much of that topography coincides with faults and folds that continue into the overlying sedimentary rocks, making it difficult to assess how much of it originates from the earlier pillow stage. This highlights the benefits of studying shallow evaporites such as those in the Red Sea, which do not suffer from this problem so greatly. Nevertheless, those Santos Basin data contain some examples where stratigraphy closely above the evaporites is discordant with a more rugged evaporite surface (Guerra and Underhill, 2012, their figures 7, 8; Jackson et al., 2015a, their figures 7a, 8c), suggesting that some relief of up to ~100 m from that earlier stage has been preserved.

5.2. Vertical evaporite movements driven by anhydrite and other non-halite components (internal density variations)?

Tectonic growth stratigraphy within evaporite is evidence that vertical differential movements (diapirism) occurred during evaporite deposition in the Red Sea. Tectonic growth stratigraphy within evaporite sequences can also be inferred from seismic reflection data from the Levant (Gvirtzman et al., 2013; Hübscher and Netzeband, 2007; Netzeband et al., 2006; Reiche et al., 2014), North Sea Zechstein (Clark et al., 1998; Joffe et al., 2021) and Santos (Davison et al., 2012; Mann and Rigg, 2012; Mohriak et al., 2012) basins. The vertical differential movements producing growth stratigraphy are difficult to explain by loading of the evaporites by overlying sediments where those sediments have lower density than halite (Hudec et al., 2009). Although other mechanisms may be involved as we explore later, diapirism in the Red Sea potentially originates from deposition of anhydrite and other lithologies denser than halite in mini-basins, which now form the regions of layered evaporites. Diapirs (transparent evaporites) then developed by "downbuilding" (Nikolinakou et al., 2017) during the late Miocene, while layered evaporites were deposited around them. We first consider the magnitudes of vertical movements.

Only a few hundred metres of layered evaporites were sampled by the DSDP (Figure 2) so it may not be typical of the deep-water Zeit Formation, though we use the data from those sites to assess the order of magnitude of density contrast between layered evaporites and massive halite. Assigning the lithologies below the Miocene-Pliocene boundary of Sites

225 and 227 (Figure 2) the density ~2 g/cm^3 for the shale (Figure 3) and mean densities of halite (2.145 g/cm^3) and anhydrite (2.857 g/cm^3) of the DSDP sample measurements from the sites (Wheildon et al., 1974), the mean densities of those layered evaporites are estimated to be 2.56 g/cm^3 (Site 225), 2.29 g/cm^3 (Site 227) and 2.37 g/cm^3 (with lithologies of Sites 225 and 227 combined).

The importance of these densities can be assessed by carrying out a simple isostatic balance calculation, idealising the layered evaporites as effectively floating on and within the weaker massive halite. The mass density in a column of layered evaporite of 2.37 g/cm^3 average density can then be equated with that of a column of pure halite rising an additional height *Z* above the level of the layered evaporites, with both bodies in water of density 1.0 g/cm^3 (Figure 12). The two columns balance isostatically if their total weights are the same at their base. Such a structure is stable if the depth extent of the layered evaporites is:

$$H = Z\frac{(\rho_L - \rho_H)}{(\rho_L - \rho_w)} - Z \qquad (3)$$

Using 274 m (=2σ from the variogram modelling) as a typical measure of evaporite relief *Z*, we estimate *H*=1400 m using the above densities. The thickness of Plio-Pleistocene sediments has been ignored, as they mostly drape the underlying S-reflection (Mitchell et al., 2019) and thus load the underlying structure uniformly. However, the extent to which they do preferentially infill basins will lead to an over-estimate of *Z* and thus *H*.

For comparison, the average thickness of the evaporite layer (both layered and massive) is 3760 m for the segments of the Izzeldin data analysed numerically. The depth extent of layered evaporites in the deep-seismic image in Figure 4g is difficult to assess because they are variably obscured by multiple reflections but interpretations of the higher quality seismic images of Colombo et al. (2014) located in Figure 1 were corroborated by electrical resistivity models. They suggest that the layered evaporites extend significantly below 1400 m and in one case towards 3000 m depth. A further body of layered evaporites off the northern Red Sea Arabian coast exceeds 4000 m depth (Rowan, 2014). If those thicknesses are representative of the central Red Sea, the layered evaporites on average have a mean density below 2.37 g/cm^3 and hence a larger halite component than suggested by the DSDP cores. Alternatively, if the layered evaporites reach the underlying basement and fully displace the halite (Rowan, 2014), they can be supported by basement rigidity and hence have a significantly greater density.

5.3. Significance of only weak periodicity

The finding that the evaporite surface or S-reflection is better described as stochastic than periodic agrees with the earlier finding of Hernandez (2020) for seismic datasets from other basins involving more deeply buried evaporites. Somewhat as Hernandez (2020) found from those datasets, the Red Sea evaporite surface shows no strongly dominating wavelength above 13 km and below that wavelength a linear variation in spectral power with frequency. Although we do not describe the evaporite surface topography as a fractal, the data nevertheless do not possess characteristic wavelengths, but rather a range of wavelengths, as do fractals (Turcotte, 1991). This is incompatible with Rayleigh-Taylor diapirism models involving fluids of contrasting density, which predict regularly spaced diapirs (Fernandez and Kaus, 2015; Hughes and Davison, 1993; Turcotte and Schubert, 1982).

As modifying the Rayleigh-Taylor model to include a plastic overburden leads to multiple wavelengths of diapirism being predicted (Ismail-Zadeh et al., 2002), perhaps the varied and higher viscosity of the layered evaporites provides effective yield strength, leading to multiple wavelengths of diapirism of the mostly underlying Mid-Miocene halites? Rowan et al. (2019) noted that anhydrite tends to behave more viscously under extension, commonly forming stringers. There is some evidence of faults affecting the layered evaporites, such as the abrupt termination of the S-reflection where marked "F" in Figure 4a and elsewhere in the *Urania* seismic data (Mitchell et al., 2010), as well as abrupt curvilinear planform features in the *Urania* multibeam data. Extension of an upper, more rigid layer over halite ("reactive diapirism") was explored by Vendeville and Jackson (1992). A stochastic distribution of faults at mid-ocean ridges has been shown to generate fractal-like topography (Malinverno and Cowie, 1993; Malinverno and Gilbert, 1989) and thus faulting might partly explain the lack of periodicity.

However, seismic images such as Figure 4g and those in references cited earlier suggest that the layered evaporites are largely folded, rather than faulted. The lack of a characteristic wavelength therefore indicates a lack of scale to that folding. We interpret the folding as caused by loading by the denser anhydrite-rich layered deposits and by widespread extension as the evaporites have flowed to the spreading axis, allowing diapirs of halite-dominated evaporites to rise between more coherent layered evaporites (Colombo et al., 2014; Izzeldin, 1987). In other salt provinces, strengthening of fold synclines by deposition and lithification of terrigenous sediments has been suggested to increase the dominant fold wavelength over time (Bochi do Amarante et al., 2021; Fort et al., 2004).

If anhydrite deposition were the main cause of layered evaporite folding in the Red Sea as we suggest, the question arises as to whether such deposition initiated at the start of the Zeit with a range of length scales, also influencing the present varied length scales of the S reflection topography. Crossley et al. (1992) reconstructed the physiography of the top of the Miocene evaporites, showing large depressions filled with mud and sand. As mentioned earlier, the varied presence of erosional surfaces (Figure 8) and varied sizes of segments of layered evaporites without erosion at S in the seismic images (Figure 4) also suggests that the S reflection surface had some relief by the end of the Miocene.

Perhaps mini-basins of the Late Miocene (Zeit Formation) layered evaporites formed over small depressions in the massive halites of the Mid-Miocene, leading to contrasts in column-averaged density between lows and highs, which drove continual diapirism during deposition. Hughes and Beydoun (1992) interpreted the biostratigraphy in commercial wells as revealing a deep (>200 m) or moderately deep marine environment in most of the Red Sea from the late early Miocene to Mid-Miocene. This is corroborated by the few quality deep-seismic data publicly available, which do not typically show erosional unconformities deeper within the evaporites (Colombo et al., 2014; Izzeldin, 1987; Rowan, 2014), suggesting they were continually submerged. As the Mid-Miocene evaporites were about half the thickness of the modern evaporites, the relief of the underlying basement may have more easily influenced halokinetic movements, such as above faults (Bochi do Amarante et al., 2021; Harding and Huuse, 2015; Koyi et al., 1993; Remmelts, 1995; Warsitzka et al., 2015). Limited high-quality seismic data that are publicly available show some transparent evaporites (i.e., halite) above basement faults (Colombo et al., 2014; Ligi et al., 2019b). As faults tend to have irregularly distributed (Cowie, 1998; Malinverno and Gilbert, 1989), this process could lead to a stochastic distribution of mini-basins.

Could continental rift faults have also still been active in the Mid-Miocene and influenced early diapirism? Normal fault movements would change the potential energy difference of evaporites and overburden across them and have been suggested or inferred elsewhere to trigger diapirism (Harding and Huuse, 2015; Nilsen et al., 1995; Vendeville et al., 1995; Withjack and Callaway, 2000). The continental rifting phase of the central Red Sea is roughly constrained by a symmetrical Chron 5 magnetic anomaly, which suggests that the rift to oceanic spreading transition occurred at ~10 Ma (Okwokwo et al., 2022). Transitions also occur in crustal seismic velocity (Egloff et al., 1991; Tramontini and Davies, 1969) and basement morphology (Izzeldin, 1987) at about the same distance from the spreading centres to the Chron 5 anomaly, corroborating this as the continental rifting to seafloor spreading transition. For comparison, the main halite deposition phase occurred through the Mid-Miocene in the South Gharib and time-equivalent formations (Hughes and Beydoun, 1992). According to a chronology presented by Hughes and Johnson (2005), they would have been deposited from 14 to 10.5 Ma. It therefore seems likely that basement faults would have been active during the Mid-Miocene halite deposition and could have influenced diapirism. The lack of diapiric lengthscale could therefore in turn also reflect a non-uniform fault distribution (Cowie, 1998; Malinverno and Gilbert, 1989).

Anhydrite preferentially accumulating in depressions contrasts with a result of Biehl et al. (2014), who showed that anhydrite in the Zechstein of the Netherlands was originally deposited as gypsum on topographic highs, which they attributed to an effect of brines rising above the level of the high. In the Red Sea, we suggest that the Late Miocene brines remained predominantly in shallow depressions, leading to precipitation of primary anhydrite or gypsum which later transformed to anhydrite (Warren, 2006), as suggested by gypsum pseudomorphs in the DSDP cores (Stoffers and Kühn, 1974). Anhydrite/gypsum and mud later forming shale were inhibited from depositing over diapirs, perhaps because of currents caused by sea surface winds or even surface waves. Furthermore, density stratification within the Red Sea may have been promoted by a change in climate. Some have suggested that the Late Miocene was wetter (Griffin, 1999), although this is not a consensus view (Fauquette et al., 2006; Pound et al., 2012). Alternatively, inflow of global sea water into the basin became more efficient, leading to less extreme salinity. In either case, anhydrite and gypsum precipitate from seawater at lower salinities than halite (Warren, 2006), so the change from massive halite to layered evaporites from the Mid-Miocene to Late Miocene (Hughes and Beydoun, 1992) implies that Red Sea salinities decreased overall.

5.4. Diapirism variably continuing into the Plio-Pleistocene (PP)

The continuation of growth stratigraphy observed in the layered evaporites into the PP and elsewhere the observed growth stratigraphy terminating at the S-reflection suggests a heterogeneity in salt-tectonic movements. Heterogeneity could partly have arisen from different dynamic causes of the movements. For example, anhydrite deposition between halite-rich diapirs would have stopped at the end of the Miocene and hemipelagics later deposited there would have added less load because of their lower density (Figure 3). In contrast, movements of the evaporites towards the spreading axis and deeps causing extension and diapirism has likely been more persistent. As the evaporite flow fronts overlie oceanic crust younger than 5.3 Ma (Mitchell et al., 2021; Okwokwo et al., 2022) and in places to the spreading axis (Augustin et al., 2014; Augustin et al., 2016), that movement continued after the Miocene. Alternatively, the varied presence of growth stratigraphy reflects changes in dominant wavelength of folding over time as mini-basins became more rigid (Bochi do Amarante et al., 2021; Fort et al., 2004). These comments suggest that further imaging seismically the growth stratigraphy within the PP and dating that stratigraphy could potentially reveal interesting details of the post-Miocene evaporite movements.

5.5. Are the Red Sea evaporites effective analogues of the earlier Santos evaporites?

If the Red Sea evaporites were useful analogues of those of the Santos and other basins in their earlier pillow stages, the detailed stratigraphy revealed here would provide clues to the early structures of the older basins that are now difficult to discern because their evaporites are deeply buried, less well imaged and more strongly deformed. Evaporite structures in such "salt giants" have been expected to evolve by pillows (small-amplitude undulations) becoming accentuated by deposition of denser terrigenous sediment in mini-basins between them (Fernandez and Kaus, 2015; Nikolinakou et al., 2017), thus the spacings of pillows could indicate the spacings of diapirs that develop from them (Hughes and Davison, 1993). However, there are a number of complications to this evolution (Hernandez, 2020). The early sediments deposited over evaporites have commonly lower density than halite, suggesting that other causes of diapirism are more important (Hudec et al., 2009). According to Waltham (1997), buoyancy only becomes an important driver of diapirism at spatial wavelengths of 12 km and greater.

Seismic stratigraphy immediately above the thickened evaporites of the São Paulo Plateau suggests that most of the diapiric movements occurred up until the Maastrichtian but after then sediments accumulated with less diapirism-related deformation (Pichel et al., 2017; Quirk et al., 2013). The topography of the base of evaporite sequences has been suggested to be important for initiating diapirism, in particular, fault scarps (Koyi et al., 1993; Remmelts, 1995; Warsitzka et al., 2015). There is evidence of such effects in the Santos Basin (Pichel et al., 2018), although generally there is only a weak correspondence between the positions of diapirs and underlying topography (Davison et al., 2012; Pichel et al., 2018). That might be a result of lateral translation of the evaporites (Alves et al., 2017; Pichel et al., 2018), but we suggest that diapirism may have also been affected by density and rheological variations within the evaporites, as we interpret for the Red Sea evaporites. Subsidence of the layered denser evaporites relative to halite would have stopped once the bases of layered evaporites reached basement below the Aptian layer, as appears to be presently the case from higher quality seismic reflection data showing layering extending to the evaporite base (Davison et al., 2012). The reduction of diapiric movements at the Maastrichtian could then be explained by the end of expulsion of halite from beneath subsiding areas. If correct, modelling of the effects of evaporite movements over basement topography (Dooley et al., 2018; Pichel et al., 2019; Warsitzka et al., 2015; Warsitzka et al., 2021) may be improved if varied effective viscosity of the evaporites were incorporated.

Did these early evaporite surfaces have significant relief and if so what were its consequences? A reconstruction by Bochi do Amarante et al. (2021) for the Upper Albian in the present-day compression zone of the Santos evaporites (their figure 10e) suggests that the top of the evaporites had a relief that was comparable to that of the Red Sea evaporites. In contrast, overlying Albian sediments are shown with a smoother surface, mostly filling underlying depressions rather than draping the evaporite topography as would be expected of purely pelagic accumulation (Tominaga et al., 2011). One lensoid part of that unit is somewhat reminiscent of contourites (Faugères et al., 1999). For comparison, reflections in the lower part of the PP in Figure 4f (marked "Contourites") are discordant with underlying S and would be lensoid if S were flatter than it is at present. Although these sediments likely have lower density than halite, contourite deposits can have significant positive relief and hence thicknesses of ~200 m as in Figure 4f would generate ~2 MPa of vertical stress. Perhaps this stress was enough to deform halite and cause subsidence in the underlying evaporites, partly explaining the growth stratigraphy within the underlying underlying evaporites marked in Figure 4f. This illustrates how an early relief of evaporite surfaces in salt giants can guide sediment transport by various processes and, in some cases, influence the later deformation.

6. Conclusions

Analyses of the early "pillow" stage of diapirism of halite-dominated evaporites in "salt giants" without overburden loading is best carried out in deposits with little overlying sediment, such as those in the Red Sea. This is made straightforward in the Red Sea by the widespread presence of a prominent seismic reflection "S" marking the top of the evaporites. The following are observed from this reflection.

Power spectra and variograms of S in the Red Sea reveal a lack of any dominant wavelength, arguing against simple Rayleigh-Taylor diapirism locally. Variograms reveal a stochastic topography with an average range of ~3.0 km over which the topography is decorrelated. Power spectra show an inverse power-law gradient for wavelengths from 1 to 13 km. At wavelengths longer than 13 km, the spectra flatten, as might be expected from weakness of halite preventing the development of topography at larger scales.

The lack of dominant wavelength is speculated to reflect effects of brittle deformation and folding of anhydrite-bearing Late Miocene evaporites. The available seismic reflection data suggest that folding dominates these evaporites. If that folding originates from deposition of denser anhydrite in mini-basins, varied length scales of topography of the Mid-Miocene evaporites may have provided the initial conditions over which varied length scales of aragonite deposition occurred in the Late Miocene, ultimately leading to the present stochastic topography of the S reflection. Alternatively, varied length scales arise from dominant wavelengths of folding changing with progressive strengthening of synclines of stronger anhydrite-dominated evaporites. Basement topography may have also influenced diapirism. Continental rift faults may have still been active during the main halite deposition phase of the Mid-Miocene, also promoting diapirism with varied lengthscales.

High-resolution seismic records show that this folding in some areas stopped at about the Miocene-Pliocene boundary, while in others it continued into the Plio-Pleistocene, suggesting that halokinetic movements were heterogeneous. Such heterogeneity could originate from varied dynamic origins of the deformation, which include the aragonite deposition (which stopped at the end of the Miocene) and widespread flowage of the evaporites towards the spreading centres (which continued into the Plio-Pleistocene), or changes in dominant fold wavelength.

Data availability

The research presented in the article is based on seismic reflection data that are not in the public domain or are already accessible in the article (Figure 4). Upon reasonable request, the derived data such as the grid in Figure 1 and profiles in Figure 6 can be made available by the first author to researchers. The DSDP data in Figure 3 are available through the geomapapp (www.geomapapp.org).

Declaration of Competing Interests

The authors declare that they have no known competing financial interests or personal relationships that influenced the work reported in this article.

Acknowledgements

We thank Rose Anne Weissel for help in locating and scanning the RV *Robert Conrad* data used in this study. We thank also the crew on RV Pelagia expedition 64PE-445 for their help in collecting the data shown in Figure 4f. That expedition ("Saltax") was funded by the GEOMAR Helmholtz Centre for Ocean Research Kiel, Germany, with participation of NCM funded by the Royal Society (International Exchange programme grant IES/R3/170081). The *Urania* cruise was funded by the Consiglio Nazionale delle Ricerche under project LEC-

EMA21F of the European Science Foundation programme EUROMARGINS (contract ERAS-CT-2003-980409 of the European Commission, DG Research FP6). Many figures shown in this article were created with the GMT free software system (Wessel and Smith, 1991). We are grateful to Schlumberger and HIS Markit for providing VISTA seismic processing software and Kingdom seismic interpretation software, respectively. We also thank an anonymous reviewer and editor Ramon Carbonell for comments that were helpful in revising the article.

References

Adamuszek, M., Tamas, D.M., Barabasch, J. and Urai, J.L., 2021. Rheological stratification in impure rock salt during long-term creep: morphology, microstructure, and numerical models of multilayer folds in the Ocnele Mari salt mine, Romania. Solid Earth, 12: 2041-2065.

Alves, T.M., Fetter, M., Lima, C., Cartwright, J.A., Cosgrove, J., Ganga, A., Queiroz, C.L. and Strugale, M., 2017. An incomplete correlation between pre-salt topography, top reservoir erosion, and salt deformation in deep-water Santos Basin (SE Brazil). Mar. Pet. Geol., 79: 300-320.

Augustin, N., Devey, C.W., van der Zwan, F.M., Feldens, P., Tominaga, M., Bantan, R. and Kwasnitschka, T., 2014. The transition from rifting to spreading in the Red Sea. Earth Planet. Sci. Lett., 395: 217-230.

Augustin, N., Mitchell, N.C., van der Zwan, F.M. and shipboard_scientific_party, 2019. RV Pelagia Fahrtbericht / Cruise Report 64PE-445: SALTAX: Geomorphology and geophysics of submarine salt flows in the Red Sea Rift, Limassol (Cyprus) – Safaga

(Egypt), 27.08. – 21.09.2018, GEOMAR Helmholtz-Zentrum für Ozeanforschung, Kiel, Germany, 46.

Augustin, N., van der Zwan, F.M., Devey, C.W., Ligi, M., Kwasnitschka, T., Feldens, P., Bantan, R. and Basaham, A.S., 2016. Geomorphology of the central Red Sea Rift: Determining spreading processes. Geomorph., 274: 162-179.

Bell, T.H., 1975. Statistical features of sea-floor topography. Deep-Sea Res., 22: 883-892.

Berner, H., Ramberg, H. and Stephansson, O., 1972. Diapirism in theory and experiment. Tectonophys., 15: 197-218.

Biehl, B.C., Reuning, L., Strozyk, F. and Kukla, P.A., 2014. Origin and deformation of intra-salt sulphate layers: an example from the Dutch Zechstein (Late Permian). Int. J. Earth Sci., 103: 697-712.

Biot, M.A. and Odé, H., 1965. Theory of gravity instability with variable overburden and compaction. Geophysics, 30: 213-227.

Bochi do Amarante, F., Jackson, C.A.-L., Pichel, L.M., Marlon dos Santos Scherer, C. and Kuchle, J., 2021. Pre-salt rift morphology controls salt tectonics in the Campos Basin, offshore SE Brazil. Basin Res., 33: 2837-2861.

Bonatti, E., Ball, M. and Schubert, C., 1970. Evaporites and continental drift. Naturwissenschaften, 57(3): 107-108.

Bonatti, E., Colantoni, P., Della Vedova, B. and Taviani, M., 1984. Geology of the Red Sea transitional zone (22°N-25°N). Oceanologica Acta, 7: 385-398.

Clark, J.A., Stewart, S.A. and Cartwright, J.A., 1998. Evolution of the NW margin of the North Permian Basin, UK North Sea. J. Geol. Soc., 155: 663-676.

Cochran, J.R., 2005. Northern Red Sea: Nucleation of an oceanic spreading center within a continental rift. Geochemistry, Geophysics, Geosystems, 6: Paper Q03006, doi:03010.01029/02004GC000826.

Cochran, J.R. and Karner, G.D., 2007. Constraints on the deformation and rupturing of continental lithosphere of the Red Sea: the transition from rifting to drifting. In: G.D. Karner, G. Manatschal and L.M. Pinheiro (Editors), Imaging, mapping and modelling continental lithosphere extension and breakup, Spec. Publ. 282. Geological Society, London, London, pp. 265 - 289.

Colombo, D., McNeice, G., Raterman, N., Zinger, M., Rovetta, D. and Sandoval Curiel, E., 2014. Exploration beyond seismic: The role of electromagnetics and gravity gradiometry in deep water subsalt plays of the Red Sea. Interpretation, 2: SH33-SH53.

Cooley, J.W. and Turkey, J.W., 1965. An algorithm for the machine calculation of complex Fourier series. Mathematics of Computation, 19: 297-301.

Cowie, P.A., 1998. Normal fault growth in three dimensions in continental and oceanic crust. In: W.R. Buck, P.T. Delaney, J.A. Karson and Y. Lababrielle (Editors), Faulting and magmatism at mid-ocean ridges. American Geophysical Union, Washington, D. C., pp. 325-348.

Crossley, R., Watkins, C., Raven, M., Cripps, D., Carnell, A. and Williams, D., 1992. The sedimentary evolution of the Red Sea and Gulf of Aden. J. Petrol. Geol., 15: 157-172.

Davis, J.C., 2002. Statistics and data analysis in geology. John Wiley, New York, 638 pp.

Davison, I., 2007. Geology and tectonics of the South Atlantic Brazilian salt basins. In: A.C. Ries, R.W.H. Butler and R.H. Graham (Editors), Deformation of the continental crust: The legacy of Mike Coward, Geol. Soc. Lond. Spec. Publ. 272., pp. 345-359.

Davison, I., Anderson, L. and Nuttall, P., 2012. Salt deposition, loading and gravity drainage in the Campos and Santos salt basins. In: G.I. Alsop, S.G. Archer, A.J. Hartley, N.T. Grant and R. Hodgkinson (Editors), Salt tectonics, sediments and prospectivity, Geol. Soc. Lond. Spec. Publ. 363., pp. 159-173.

Dooley, T.P., Hudec, M.R., Pichel, L.M. and Jackson, M.P.A., 2018. The impact of base-salt relief on salt flow and suprasalt deformation patterns at the autochthonous, paraautochthonous and allochthonous level: insights from physical models. In: K.R. McClay and J.A. Hammerstein (Editors), Passive margins: tectonics, sedimentation and magmatism, Geol. Soc. Lond. Spec. Publ. 476. pp. 287-315.

Dorner, D., Röller, K. and Stöckhert, B., 2014. High temperature indentation creep tests on anhydrite - a promising first look. Solid Earth, 5: 805-819.

Drake, C.L. and Girdler, R.W., 1964. A Geophysical Study of the Red Sea. Geophys. J. Roy. Astr. Soc., 8: 473-495.

Egloff, F., Rihm, R., Makris, J., Izzeldin, Y.A., Bobsien, M., Meier, K., Junge, P., Noman, T. and Warsi, W., 1991. Contrasting structural styles of the eastern and western margins of the southern Red Sea: the 1988 SONNE experiment. Tectonophys., 198: 329-353.

Ehrhardt, A. and Hübscher, C., 2015. The northern Red Sea in transition from rifting to drifting - lessons learned from ocean deeps. In: N.M.A. Rasul and I.C.F. Stewart (Editors), The Red Sea: The formation, morphology, oceanography and environment of a young ocean basin. Springer Earth System Sciences, Berlin Heidelberg., pp. 99-121.

Evans, R., 1978. Origin and significance of evaporites in basins around Atlantic margin. Bulletin of the American Association of Petroleum Geologists, 62: 223-234.

Faugères, J.-C., Stow, D.A.V., Imbert, P. and Viana, A., 1999. Seismic features diagnostic of contourite drifts. Mar. Geol., 162: 1-38.

Fauquette, S., Suc, J.-P., Bertini, A., Popescu, S.-M., Warny, S., Taoufiq, N.B., Villa, M.-J.P., Chikhi, H., Feddi, N., Subally, D., Clauzon, G. and Ferrier, J., 2006. How much did climate force the Messinian salinity crisis? Quantified climatic conditions from pollen records in the Mediterranean region. Paleogeography, Palaeoclimatology, Palaeoecology, 238: 281-301.

Feldens, P. and Mitchell, N.C., 2015. Salt flows in the central Red Sea. In: N.M.A. Rasul and I.C.F. Stewart (Editors), The Red Sea: The formation, morphology, oceanography and environment of a young ocean basin. Springer Earth System Sciences, Berlin Heidelberg, pp. 205-218.

Feldens, P., Schmidt, M., Mücke, I., Augustin, N., Al-Farawati, R., Orif, M. and Faber, E., 2016. Expelled subsalt fluids form a pockmark field in the eastern Red Sea. Geo-Mar. Lett., 36: 339-352.

Fernandez, N. and Kaus, B.J.P., 2015. Pattern formation in 3-D numerical models of down-built diapirs initiated by a Rayleigh–Taylor instability. Geophys. J. Int., 202: 1253-1270.

Fiduk, J.C. and Rowan, M.G., 2012. Analysis of folding and deformation within layered evaporites in Blocks BM-S-8 & -9, Santos Basin, Brazil. In: G.I. Alsop, S.G. Archer, A.J. Hartley, N.T. Grant and R. Hodgkinson (Editors), Salt tectonics, sediments and prospectivity, Geol. Soc. Lond. Spec. Publ. 363., pp. 471-487.

Fort, X., Brun, J.-P. and Chauvel, F., 2004. Salt tectonics on the Angolan margin, synsedimentary deformation processes. Am. Assoc. Pet. Geol. Bull., 88: 1523-1544.

Fox, C.G. and Hayes, D.E., 1985. Quantitative methods for analyzing the roughness of the seafloor. Rev. Geophys., 23: 1-48.

Gaulier, J.M., LePichon, X., Lyberis, N., Avedik, F., Gely, L., Moretti, I., Deschamps, A. and Hafez, S., 1988. Seismic study of the crustal thickness, Northern Red Sea and Gulf of Suez. Tectonophys., 153: 55-88.

Gilbert, L.E. and Malinverno, A., 1988. A characterization of the spectral density of ocean floor topography. Geophys. Res. Lett., 15: 1401-1404.

Girdler, R.W. and Whitmarsh, R.B., 1974. Miocene evaporites in Red Sea cores, their relevance to the problem of the width and age of oceanic crust beneath the Red Sea. In: R.B. Whitmarsh, O.E. Weser, D.A. Ross, et al. (Editors), Initial Reports of the Deep Sea Drilling Project, Vol. 23. U.S. Govt. Printing Office, Washington, D.C., pp. 913-921.

Griffin, D.L., 1999. The late Miocene climate of northeast Africa: unravelling the signals in the sedimentary succession. J. Geol. Soc. Lond., 156: 817-826.

Guennoc, P., Pautot, G., LeQentrec, M.-F. and Coutelle, A., 1990. Structure of an early oceanic rift in the northern Red Sea. Oceanologica Acta, 13: 145-157.

Guennoc, R., Pautot, G. and Coutelle, A., 1988. Surficial structures of the northern Red Sea axial valley from 23°N to 28°N: time and space evolution of the neooceanic structures. Tectonophysics, 153: 1-23.

Guerra, M.C.M. and Underhill, J.R., 2012. Role of halokinesis in controlling structural styles and sediment dispersal in the Santos Basin, offshore Brazil. In: G.I. Alsop, S.G. Archer, A.J. Hartley, N.T. Grant and R. Hodgkinson (Editors), Salt Tectonics, Sediments and Prospectivity, Geol. Soc. Lond. Spec. Publ. 363., pp. 175-206.

Gvirtzman, Z., Reshef, M., Buch-Leviatan, O. and Ben-Avraham, Z., 2013. Intense salt deformation in the Levant Basin in the middle of the Messinian Salinity Crisis. Earth Planet Sci. Lett., 379: 108-119.

Hangx, S.J.T., Spiers, C.J. and Peach, C.J., 2010. Mechanical behavior of anhydrite caprock and implications for CO2 sealing capacity. J. Geophys. Res., 115: article B07402, doi:07410.01029/02009JB006954.

Harding, R. and Huuse, M., 2015. Salt on the move: Multi stage evolution of salt diapirs in the Netherlands North Sea. Marine Pet. Geol., 61: 39-55.

Hernandez, K., 2020. Three-dimensional seismic reflection data and core information from the Dutch North Sea, the geometry and topography of salt deformation features, University of Manchester, 188 pp.

Hernandez, K., Mitchell, N.C. and Huuse, M., 2018. Deriving relationships between diapir spacing and salt-layer thickness in the Southern North Sea. In: B. Kilhams, P.A. Kukla, S. Mazur, T. McKie, H.F. Mijnlieff and K. van Ojik (Editors), Mesozoic resource potential in the Southern Permian Basin, Geol. Soc. Lond. Spec. Publ. 469., pp. 119-137.

Herzfeld, U.C., 1993. A method for seafloor classification using directional variograms, demonstrated for data from the western flank of the Mid-Atlantic Ridge. Math. Geol., 25(7): 901-924.

Herzfeld, U.C., Kim, I.I. and Orcott, J.A., 1995. Is the ocean floor a fractal? Math. Geol., 27: 421-462.

Herzfeld, U.C. and Overbeck, C., 1999. Analysis and simulation of scale-dependent fractal surfaces with application to seafloor morphology. Comput. Geosc., 25: 979-1007.

Hübscher, C. and Netzeband, G.L., 2007. Evolution of a young salt giant: The example of the Messinian evaporites in the Levantine Basin. In: M. Wallner, K.-H. Lux, W. Minkley and J. Hardy, H.R. (Editors), The Mechanical Behaviour of Salt – Understanding of THMC Processes in Salt. Taylor & Francis Group, London, pp. 175-184.

Hudec, M.R. and Jackson, M.P., 2011. The salt mine: A digital atlas of salt tectonics, 324 pp.

Hudec, M.R. and Jackson, M.P.A., 2006. Advance of allochthonous salt sheets in passive margins and orogens. Bulletin of the American Association of Petroleum Geologists, 90: 1535-1564.

Hudec, M.R., Jackson, M.P.A. and Shultz-Ela, D.D., 2009. The paradox of minibasin subsidence into salt: Clues to the evolution of crustal basins. Bulletin of the geological Society of America, 121: 201-221.

Hughes, G.W. and Beydoun, Z.R., 1992. The Red Sea - Gulf of Aden: biostratigraphy, lithostratigraphy and palaeoenvironments. J. Petrol. Geol., 15: 135-156.

Hughes, G.W. and Johnson, R.S., 2005. Lithostratigraphy of the Red Sea Region. GeoArabia, 10: 49-126.

Hughes, M. and Davison, I., 1993. Geometry and growth kinematics of salt pillows in the southern North Sea. Tectonophys., 228: 239-254.

Ismail-Zadeh, A.T., Huppert, H.E. and Lister, J.R., 2002. Gravitational and buckling instabilities of a rheologically layered structure: implications for salt diapirism. Geophys J. Int., 148: 288-302.

Izzeldin, A.Y., 1987. Seismic, gravity and magnetic surveys in the central part of the Red Sea: their interpretation and implications for the structure and evolution of the Red Sea. Tectonophysics, 143: 269-306.

Izzeldin, A.Y., 1989. Transverse structures in the central part of the Red Sea and implications on early stages of oceanic accretion. Geophys. J., 96: 117-129.

Jackson, C.A.-L., Jackson, M.P.A. and Hudec, M.R., 2015a. Understanding the kinematics of salt-bearing passive margins: A critical test of competing hypotheses for the origin of the Albian Gap, Santos Basin, offshore Brazil. Bulletin of the Geological Society of America, 127: 1730-1751.

Jackson, C.A.-L., Jackson, M.P.A., Hudec, M.R. and Rodriguez, C.R., 2015b. Enigmatic structures within salt walls of the Santos Basin - Part 1: Geometry and kinematics from 3D seismic reflection and well data. J. Struct. Geol., 75: 135-162.

Jackson, C.A.-L., Rodriguez, C.R., Rotevatn, A. and Bell, R.E., 2014. Geological and geophysical expression of a primary salt weld: An example from the Santos Basin, Brazil. Interpretation, 2: SM77-SM89.

Joffe, A., Jackson, C.A.-L. and Pichel, L.M., 2021. 3D seismic reflection data reveal syn-depositional halokinesis in the Zechstein Supergroup (Lopingian), Central North Sea, UK. Am. Assoc. Petrol. Geol. Bull., in review.

Knott, S.T., Bunce, E.T. and Chase, R.L., 1966. Red Sea seismic reflection studies in The World Rift System, Geol. Surv. Canada, Paper 66-14: 78-97.

Koyi, H., Jenyon, M.K. and Petersen, K., 1993. The effect of basement faulting on diapirism. J. Petrol. Geol., 16: 285-312.

Ligi, M., Bonatti, E., Bortoluzzi, G., Cipriani, A., Cocchi, L., Caratori Tontini, F., Carminati, E., Ottolini, L. and Schettino, A., 2012. Birth of an ocean in the Red Sea: Initial pangs. Geochem. Geophys. Geosys., 13: Paper Q08009, doi:08010.01029/02012GC004155.

Ligi, M., Bonatti, E., Bosworth, W., Cai, Y., Cipriani, A., Palmiotto, C., Ronca, S. and Seyler, M., 2018. Birth of an ocean in the Red Sea: Oceanic-type basaltic melt intrusions precede continental rupture. Gondwana Res., 54: 150-160.

Ligi, M., Bonatti, E. and Rasul, N., 2019a. Seafloor spreading initiation: geophysical and geochemical constraints from the Thetis and Nereus Deeps, central Red Sea. In: N.M.A. Rasul and I.C.F. Stewart (Editors), The Red Sea: The formation, morphology, oceanography and environment of a young ocean basin. Springer Earth System Science Series. Springer Nature, Switzerland, pp. 323-340.

Ligi, M., Bonatti, E., Tontini, F.C., Cipriani, A., Cocchi, L., Schettino, A., Bortoluzzi, G., Ferrante, V., Khalil, S., Mitchell, N.C. and Rasul, N., 2011. Initial burst of oceanic crust accretion in the Red Sea due to edge-driven mantle convection. Geology, 39: 1019-1022.

Ligi, M., Bosworth, W. and Ronca, S., 2019b. Oceanization starts at depth during continental rupturing in the Northern Red Sea. In: N.M.A. Rasul and I.C.F. Stewart (Editors), Geological Setting, Palaeoenvironment and Archaeology of the Red Sea. Springer Nature Switzerland, Cham, Switzerland, pp. 131-157.

Mackenzie, K.V., 1981. Discussion of sea-water sound-speed determinations. J. Acoust. Soc. Am., 70: 801-806.

Makris, J., Tsironidis, J. and Richter, H., 1991. Heatflow density distribution in the Red Sea. Tectonophys., 198: 383-393.

Malinverno, A., 1989. Segmentation of topographic profiles of the seafloor based on a self-affine model. IEEE J. Oceanic Eng., 14: 348-359.

Malinverno, A. and Cowie, P.A., 1993. Normal faulting and the topographic roughness of mid-ocean ridge flanks. J. Geophys. Res., 98: 17921-17939.

Malinverno, A. and Gilbert, L.E., 1989. A stochastic model for the creation of ocean floor topography at a slow spreading center. J. Geophys. Res., 94: 1665-1675.

Manheim, F.T., Dwight, L. and Belastock, R.A., 1974. Porosity, density, grain density, and related physical properties of sediments from the Red Sea drill cores. In: R.B. Whitmarsh, O.E. Weser, D.A. Ross, et al. (Editors), Initial Reports of the Deep Sea Drilling Project, Vol. 23. U.S. Govt. Printing Office, Washington, D.C., pp. 887-907.

Mann, J. and Rigg, J.W.D., 2012. Santos Basin: Complex salt structures and pre-salt potential revealed by new CGGVeritas 3D data. GEO ExPro, February: 36-39.

Mart, Y. and Ross, D.A., 1987. Post-Miocene rifting and diapirism in the northern Red Sea. Mar. Geol., 74: 173-190.

Martinez, F. and Cochran, J.R., 1989. Geothermal Measurements in the northern Red Sea: Implications for lithospheric thermal structure and mode of extension during continental rifting. J. Geophys. Res., 94: 12,239-212,266.

Matheron, G., 1963. Principles of geostatistics. Economic Geology, 58: 1246-1266.

Maul, A., Cetale, M., Guizan, C., Corbett, P., Underhill, J.R., Teixeira, L., Pontes, R. and González, M., 2021. The impact of heterogeneous salt velocity models on the gross rock volume estimation: an example from the Santos Basin pre-salt, Brazil. Petrol. Geosci., 27: art. petgeo2020-2105.

Mello, U.T. and Pratson, L.F., 1999. Regional slope stability and slope-failure mechanics from the two-dimensional state of stress in an infinite slope. Marine Geology, 154: 339-356.

Mitchell, N.C. and Augustin, N., 2017. Halokinetics and other features of GLORIA long-range sidescan sonar data from the Red Sea. Mar. and Pet. Geol., 88: 724-738.

Mitchell, N.C., Ligi, M., Farrante, V., Bonatti, E. and Rutter, E., 2010. Submarine salt flows in the central Red Sea. Geol. Soc. Am. Bull., 122: 701-713.

Mitchell, N.C., Ligi, M., Feldens, P. and Hübscher, C., 2017. Deformation of a young salt giant: regional topography of the Red Sea Miocene evaporites. Basin Res., 29: 352-369.

Mitchell, N.C., Ligi, M. and Rasul, N.M.A., 2019. Variations in Plio-Pleistocene deposition in the Red Sea. In: N.M.A. Rasul and I.C.F. Stewart (Editors), Geological Setting, Palaeoenvironment and Archaeology of the Red Sea. Springer Earth System Science Series. Springer Nature, Cham, Switzerland, pp. 323-340.

Mitchell, N.C., Shi, W., Izzeldin, A.Y. and Stewart, I.C.F., 2021. Reconstructing the level of the central Red Sea evaporites at the end of the Miocene. Basin Res., 33: 1266-1292, https://doi.org/1210.1111/bre.12513.

Mohriak, W.U., Szatmari, P. and Anjos, S., 2012. Salt: geology and tectonics of selected Brazilian basins in their global context. In: G.I. Alsop, S.G. Archer, A.J. Hartley, N.T. Grant and R. Hodgkinson (Editors), Salt tectonics, sediments and prospectivity, Geol. Soc. Lond. Spec. Publ. 363., pp. 131-158.

Nettleton, L.L., 1934. Fluid mechanics of salt domes. Bull. Am. Assoc. Petrol. Geol., 18: 1175-1204.

Netzeband, G.L., Hübscher, C. and Gajewski, D., 2006. The structural evolution of the Messinian evaporites in the Levantine Basin. Mar. Geol., 230: 249-273.

Nikolinakou, M.A., Heidari, M., Hudec, M.R. and Flemings, P.B., 2017. Initiation and growth of salt diapirs in tectonically stable settings: Upbuilding and megaflaps. Am. Assoc. Petrol. Geol. Bull., 101: 887-905.

Nilsen, K.T., Vendeville, B.C. and Johansen, J.-T., 1995. Influence of regional tectonics on halokinesis in the Nordkapp Basin, Barents Sea. In: M.P.A. Jackson, D.G. Roberts and S. Snelson (Editors), Salt tectonics: a global perspective: AAPG Memoir 65. Am. Assoc. Petrol. Geol., Tulsa, OK, pp. 413-436.

Okwokwo, O.I., Mitchell, N.C., Shi, W., I.C.F. Stewart and Izzeldin, A.Y., 2022. How have thick evaporites affected early sea-floor spreading magnetic anomalies in the Central Red Sea? Geophys. J. Int., in press.

Pautot, G., Auzende, J.M. and LePichon, X., 1970. Continuous deep salt layer along North Atlantic margins related to early phase of rifting. Nature, 227: 351-354.

Percival, D.B. and Walden, A.T., 1993. Spectral Analysis for Physical Applications. Cambridge University Press, New York.

Phillips, J.D. and Ross, D.A., 1970. Continuous seismic reflexion profiles in the Red Sea. Philosophical Transaction of the Royal Society, 267 series A: 143-152.

Pichel, L.M., Finch, E. and Gawthorpe, R.L., 2019. The impact of pre-salt topography on salt tectonics: A discrete-element modeling approach. Tectonics, 38: article 2018TC005174.

Pichel, L.M., Peel, F.J., Jackson, C.A. and Huuse, M., 2017. Tectono-stratigraphic development of ramp syncline basins. Am. Assoc. Pet. Geol. Search and Discovery: Article #10955.

Pichel, L.M., Peel, F.J., Jackson, C.A.-L. and Huuse, M., 2018. Geometry and kinematics of salt-detached ramp syncline basins. J. Struct. Geol., 115: 208-230.

Poliakov, A.N.B., Podladchikov, Y. and Talbot, C., 1993. Initiation of salt diapirs with frictional overburdens: numerical experiments. Tectonophys., 228: 199-210.

Pound, M.J., Haywood, A.M., Salzmann, U. and Riding, J.B., 2012. Global vegetation dynamics and latitudinal temperature gradients during the Mid to Late Miocene (15.97–5.33 Ma). Earth-Science Reviews, 112: 1-22.

Quirk, D.G., Hertle, M., Jeppesen, J.W., Raven, M., Mohriak, W.U., Kann, D.J., Nørgaard, M., Howe, M.J., Hsu, D., Coffey, B. and Mendes, M.P., 2013. Rifting, subsidence and continental break-up above a mantle plume in the central South Atlantic. In: W.U. Mohriak, A. Danforth, P.J. Post, D.E. Brown, G.C. Tari, M. Nemcok and S.T. Sinha (Editors), Conjugate divergent margins, Geol. Soc. Lond. Spec. Pub. 369, pp. 185-214.

Quirk, D.G., Schødt, N., Lassen, B., Ings, S.J., Hsu, D., Hirsch, K.K. and von Nicolai, C., 2012. Salt tectonics on passive margins: examples from Santos, Campos and Kwanza basins. In: G.I. Alsop, S.G. Archer, A.J. Hartley, N.T. Grant and R. Hodgkinson (Editors), Salt tectonics, sediments and prospectivity, Geol. Soc. Lond. Spec. Publ. 363, pp. 207-244.

Rapp, R.H., 1989. The decay of the spectrum of the gravitational potential and topography of the Earth. Geophys. J. Int., 99: 449-455.

Reiche, S., Hübscher, C. and Beitz, M., 2014. Fault-controlled evaporite deformation in the Levant Basin, Eastern Mediterranean. Mar. Geol., 354: 53-68.

Remmelts, G., 1995. Fault-related salt tectonics in the southern North Sea, The Netherlands. In: M.P.A. Jackson, D.G. Roberts and S. Snelson (Editors), Salt tectonics: a global perspective: AAPG Memoir 65, pp. 261-272.

Richter, H., Makris, J. and Rihm, R., 1991. Geophysical observations offshore Saudi Arabia: seismic and magnetic observations. Tectonophys., 198: 297-310.

Robert, A. and Richards, K.S., 1988. On modeling of sand bedforms using the semivariogram. Earth Surface Proc. Landf., 13: 459-473.

Rona, P.A., 1982. Evaporites at passive margins. In: R.A. Scrutton (Editor), Dynamics of passive margins. Am. Geophys. Union and Geol. Soc. Am., Washington, D.C., pp. 116-132.

Ross, D.A. and Schlee, J., 1973. Shallow structure and geologic development of the southern Red Sea. Geol. Soc. Am. Bull., 84: 3827-3848.

Rowan, M.G., 2014. Passive-margin salt basins: hyperextension, evaporite deposition, and salt tectonics. Basin Res., 26: 154-182.

Rowan, M.G., 2018. The South Atlantic and Gulf of Mexico salt basins: crustal thinning, subsidence and accommodation for salt and presalt strata. In: K.R. McClay and J.A. Hammerstein (Editors), Passive Margins: Tectonics, Sedimentation and Magmatism, Geol. Soc. Lond. Spec. Publ. 476, doi.org/10.1144/SP1476.1146.

Rowan, M.G., Urai, J.L., Fiduk, J.C. and Kukla, P.A., 2019. Deformation of intrasalt competent layers in different modes of salt tectonics. Solid Earth, 10: 987-1013.

Schmalholz, S.M. and Urai, J., 2014. Rheology of anhydrite during deformation in nature: a first look. Geophysical Research Abstracts, European Geoscience Union, 16: EGU2014-14871.

Searle, R.C. and Ross, D.A., 1975. A geophysical study of the Red Sea axial trough between 20.5° and 22°N. Geophys. J. Roy. Astr. Soc., 43: 555-572.

Stoffers, P. and Kühn, R., 1974. Red Sea evaporites: A petrographic and geochemical study. In: R.B. Whitmarsh, O.E. Weser, D.A. Ross, et al. (Editors), Initial Reports of the Deep Sea Drilling Project, Vol. 23. U.S. Govt. Printing Office, Washington, D.C., pp. 821-847.

Tominaga, M., Lyle, M. and Mitchell, N.C., 2011. Seismic interpretation of pelagic sedimentation regimes in the 18–53 Ma eastern equatorial Pacific: Basin-scale sedimentation and infilling of abyssal valleys. Geochem. Geophys. Geosys., 12: Paper Q03004, doi:03010.01029/02010GC003347.

Tramontini, C. and Davies, D., 1969. A seismic refraction survey in the Red Sea. Geophys. J. R. Astr. Soc., 17: 225-241.

Turcotte, D.L., 1991. Fractals in geology: What are they and what are they good for? Geol. Soc. Am. Today, 1: 1,3-4.

Turcotte, D.L., 1997. Fractals and chaos in geology and geophysics. Cambridge University Press, Cambridge, 398 pp.

Turcotte, D.L. and Schubert, G., 1982. Geodynamics: applications of continuum physics to geological problems. John Wiley and Sons, New York, 450 pp.

Uchupi, E. and Ross, D.A., 1986. The tectonic style of the northern Red Sea. Geo-Marine Letters, 5: 203-209.

Urai, J.L., Schléder, Z., Spiers, C.J. and Kukla, P.A., 2017. Flow and transport properties of salt rocks. In: R. Littke, U. Bayer, D. Gajewski and S. Nelskamp (Editors), Dynamics of complex intracontinental basins: The Central European basin system. Springer, Berlin, pp. 277-290.

Urai, J.L., Spiers, C.J., Zwart, H.J. and Lister, G.S., 1986. Weakening of rock salt by water during long-term creep. Nature, 324: 554-557.

van Dijk, T.A.G.P., Lindenbergh, R.C. and Egberts, P.J.P., 2008. Separating bathymetric data representing multiscale rhythmic bed forms: A geostatistical and spectral method compared. J. Geophys. Res., 113: article F04017, doi:04010.01029/02007JF000950.

Vendeville, B.C., Ge, H. and Jackson, M.P.A., 1995. Scale models of salt tectonics during basement-involved extension. Petrol. Geosci., 1: 179-183.

Vendeville, B.C. and Jackson, M.P.A., 1992. The rise of diapirs during thin-skinned extension. Mar. Petrol. Geol., 9: 331-353.

Waltham, D., 1997. Why does salt start to move? Tectonophys., 282: 117-128.

Warren, J.K., 2006. Evaporites: Sediments, Resources and Hydrocarbons. Springer, Berlin.

Warsitzka, M., Kley, J. and Kukowski, N., 2015. Analogue experiments of salt flow and pillow growth due to basement faulting and differential loading. Solid Earth, 6: 9-31.

Warsitzka, M., Závada, P., Jähne-Klingberg, F. and Krzywiec, P., 2021. Contribution of gravity gliding in salt-bearing rift basins - a new experimental setup for simulating salt tectonics under the influence of sub-salt extension and tilting. Solid Earth, 12: 1987-2020.

Wessel, P. and Smith, W.H.F., 1991. Free software helps map and display data. EOS, Transactions, American Geophysical Union, 72: 441.

Wheildon, J., Evans, T.R. and Girdler, R.W., 1974. Thermal conductivity, density, and sonic velocity measurements of samples of anhydrite and halite from Sites 225 and 227. In: R.B. Whitmarsh, O.E. Weser, D.A. Ross, et al. (Editors), Initial Reports of the Deep Sea Drilling Project, Vol. 23. U.S. Govt. Printing Office, Washington, D.C., pp. 909-911.

Whitmarsh, R.B., Weser, O.E. and Ross, D.A., 1974. Initial Reports of the Deep Sea Drilling Project, 23B. U. S. Government Printing Office, Washington, D. C.

Withjack, M.O. and Callaway, S., 2000. Active normal faulting beneath a salt layer: An experimental study of deformation patterns in the cover sequence. Am. Assoc. Pet. Geol. Bull., 84: 627-651.

Figures:

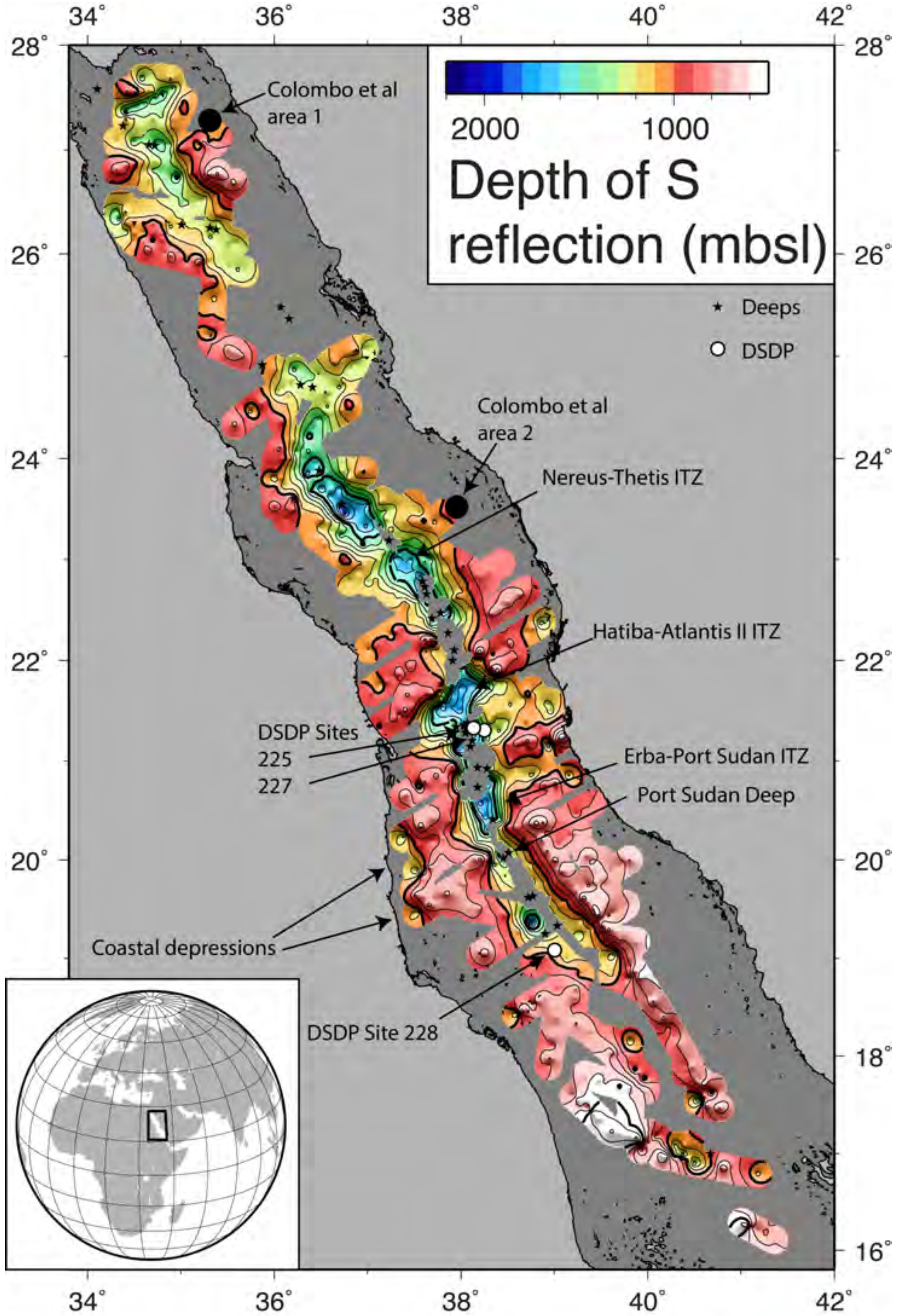

Figure 1: Depth of the S-reflection marking the top of the Miocene evaporites or close to it, contoured every 100 m (mbsl: metres below sea-level). Map shows grid of Mitchell et al. (2017) updated with 3D seismic data from offshore Egypt (Mitchell et al., 2019) and here with sparker seismic records from RV *Pelagia* (Augustin et al., 2019). Data track coverage is shown

in Figure 5. Seismic two-way times of the seabed and S-reflections were converted to depth below sea level using a water velocity of 1538 m/s derived using empirical equations (Mackenzie, 1981) and 1900 m/s for the hemipelagic Plio-Pleistocene sediments based on sample measurements (Whitmarsh et al., 1974) and seismic refraction results (Drake and Girdler, 1964; Gaulier et al., 1988). Data were binned at 0.01° X 0.01° intervals and then interpolated and extrapolated to improve visualisation over distances up to 0.15°, hence map resolution varies between these two extremes. Asterisks locate the Red Sea deeps from a catalogue of Augustin et al. (2016). Three Deep Sea Drilling Project (DSDP) sites (Whitmarsh et al., 1974) are shown. Two solid circles locate areas of geophysical data of Colombo et al. (2014) described in the text.

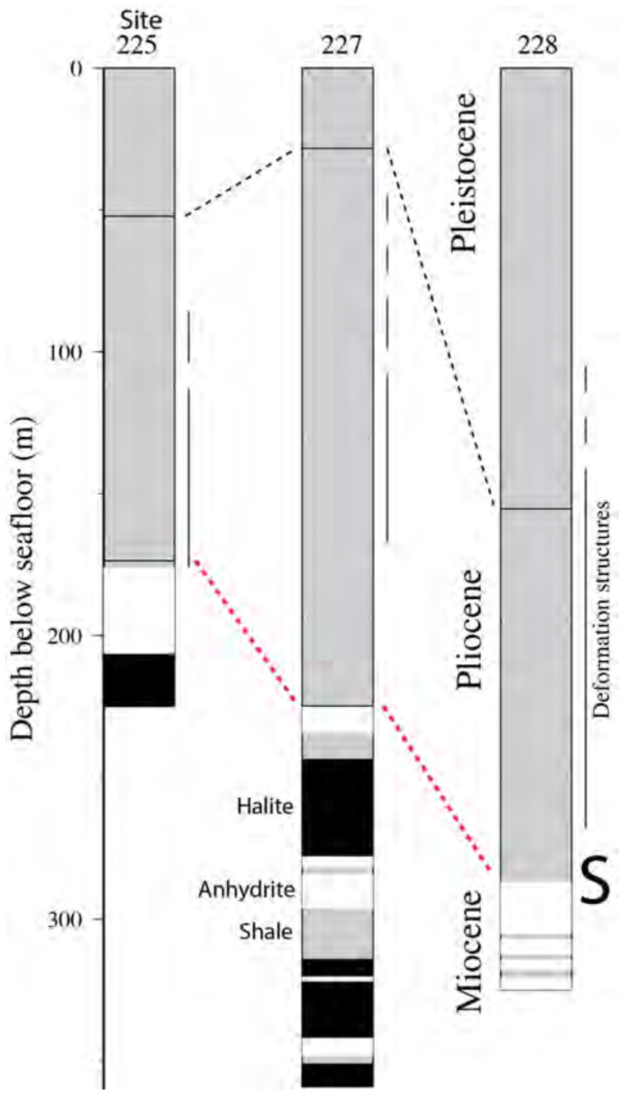

Figure 2. Summary of the stratigraphy of samples recovered at the three DSDP sites located in Figure 1 based on the interpretations of the drilling scientists (Stoffers and Kühn, 1974; Whitmarsh et al., 1974). Segments of core showing deformation structures marked by vertical bars are from Girdler and Whitmarsh (1974). S: level corresponding with the S-reflection in seismic data, which marks the top of the Miocene evaporites. Within the Miocene, black, white and grey represent halite, anhydrite and shale.

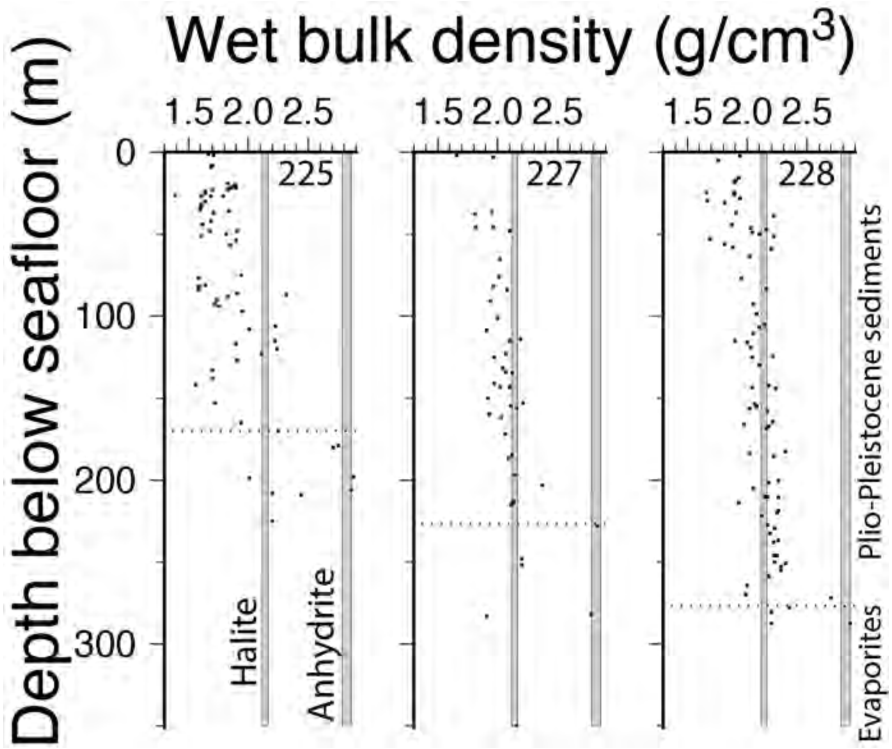

Figure 3: Sample density measurements for the three Deep Sea Drilling Project sites located in Figure 1 from Manheim et al. (1974). Vertical grey bars show the ranges of density values for all halite and anhydrite samples measured at the sites from Wheildon et al. (1974). Dotted lines mark the top of the Miocene evaporites at each site.

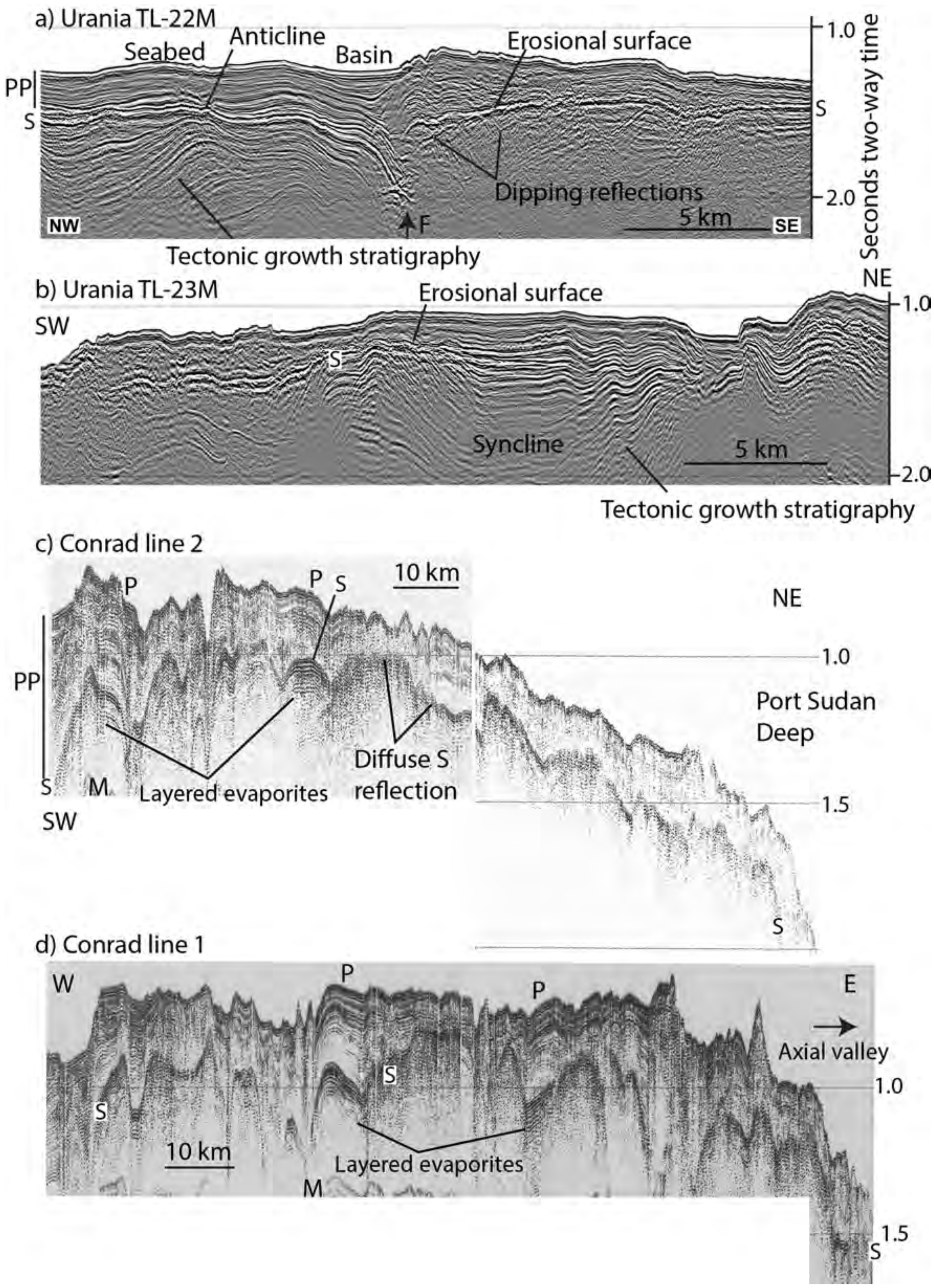
a) Urania TL-22M
Seabed
Anticline
Basin
Erosional surface
PP
S
S
Dipping reflections
NW
F
5 km
SE
1.0
2.0
Seconds two-way time
Tectonic growth stratigraphy
b) Urania TL-23M
Erosional surface
SW
NE
S
Syncline
5 km
1.0
2.0
Tectonic growth stratigraphy
c) Conrad line 2
P
P S
10 km
NE
PP
1.0
Port Sudan Deep
Diffuse S reflection
S M
Layered evaporites
SW
1.5
S
d) Conrad line 1
W
P
P
E
Axial valley
S
S
1.0
10 km
Layered evaporites
M
1.5
S

1190

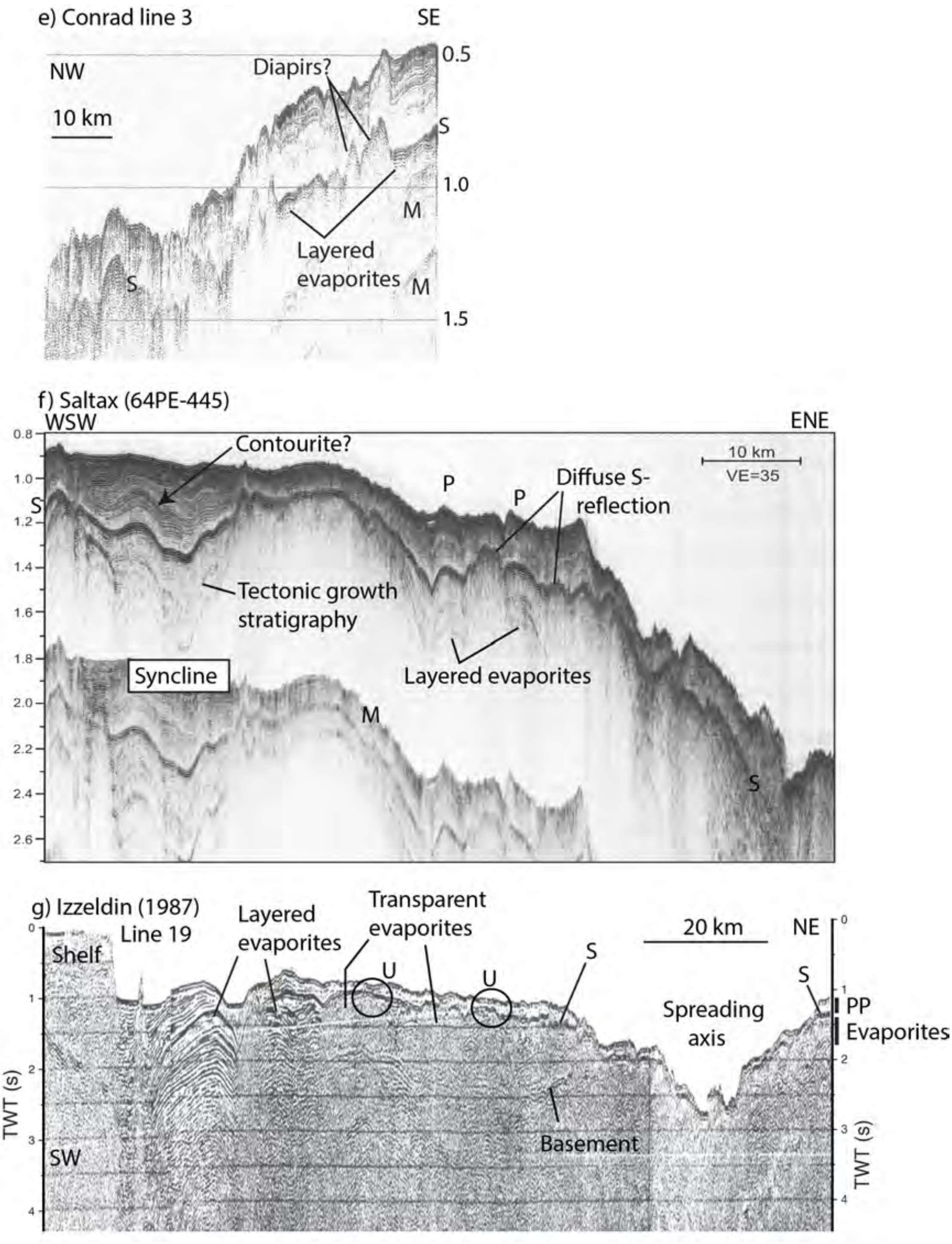

Figure 4: Example seismic reflection profiles located in Figure 5. S: reflection marking the top of the Miocene evaporites (Miocene-Pliocene boundary); PP: Plio-Pleistocene sediments; P: pelagic-like geometry of Plio-Pleistocene sediments; F: fault; U: unconformity (erosional surface).

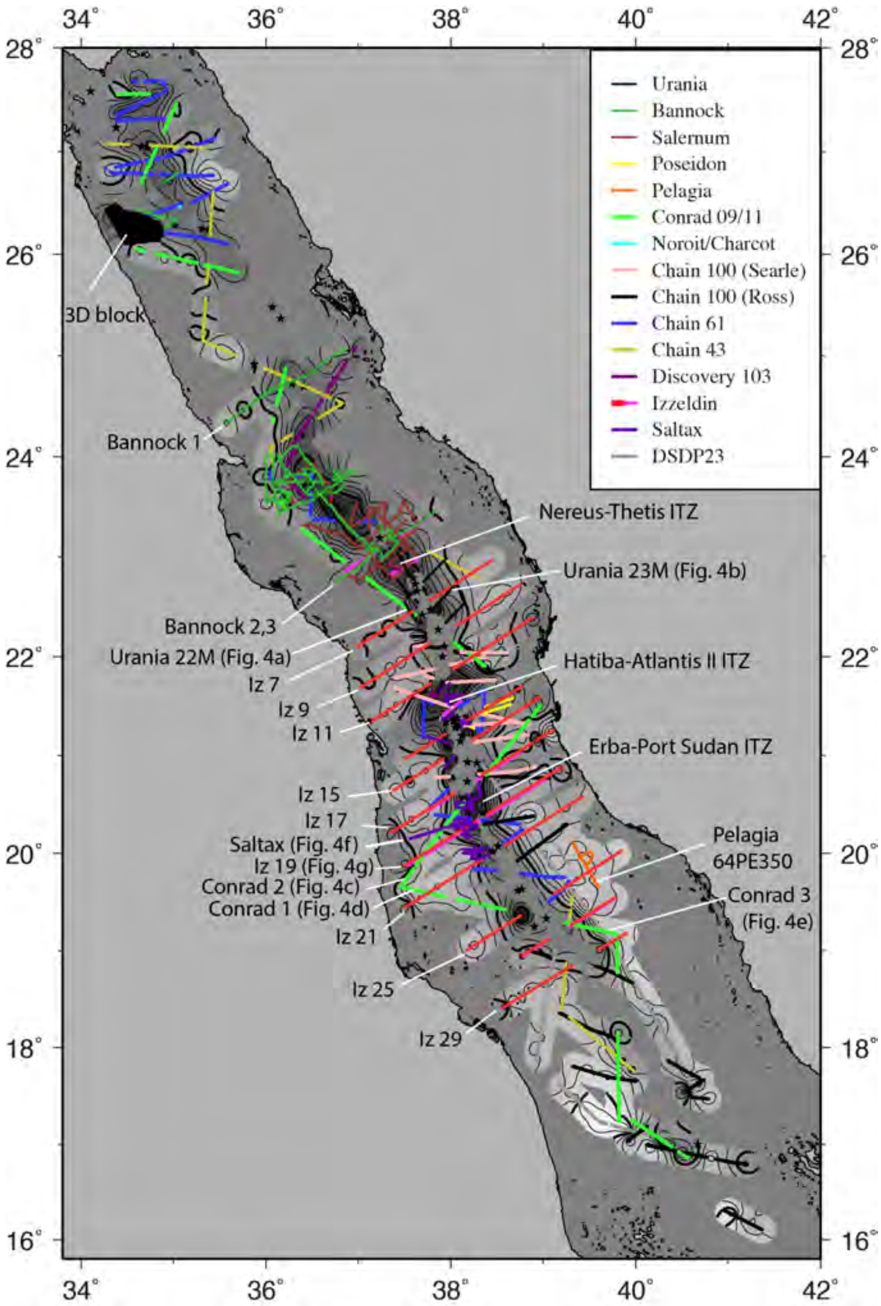

Figure 5: Locations of seismic reflection lines overlain on a grey version of the S-reflection depth map of Figure 1. ITZ: inter-trough zone. For details of original seismic data sources, see Mitchell et al. (2017). Long seismic lines selected for Figure 6 are indicated. Those marked "Iz" are lines of Izzeldin (1987).

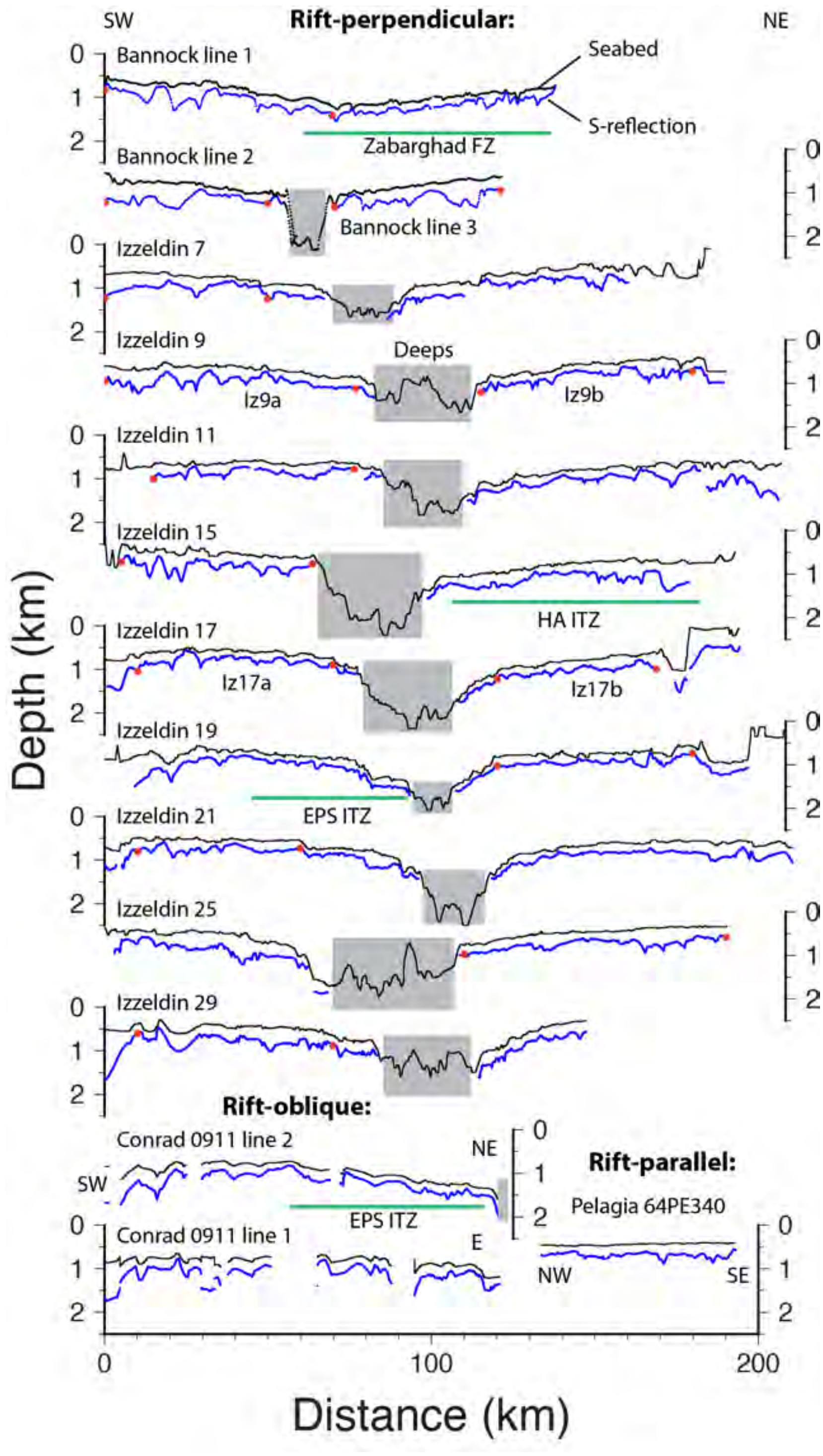

Figure 6: Profiles of seabed (black) and S-reflection (blue) topography derived from the lines located in Figure 5. Grey boxes locate deeps, which are largely without evaporites. Red circles mark ends of segments of S-reflection used to calculate the variograms in Figure 10 (where two segments are used for a line, they are indicated by abbreviated identifiers Iz9a, etc.). Green bars highlight sections of data crossing collapse structures where the evaporite surface

has deflated in response to more significant flowage into inter-trough zones. HA ITZ: Hariba-Atlantis II inter-trough zone, EPS ITZ: Erba-Port Sudan inter-trough zone.

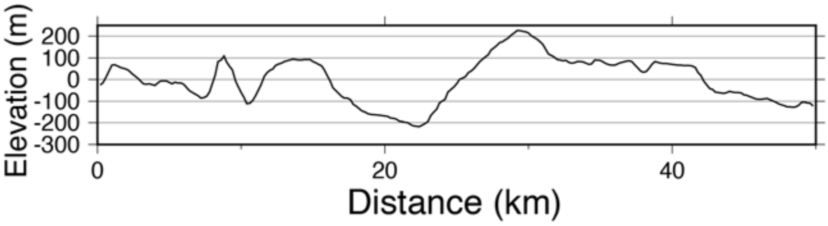

Figure 7. Example of detrended S-reflection topography from the west side of Bannock line 2 in Figure 6. "Elevation" is relative to a regression line fitted to the S-reflection topography.

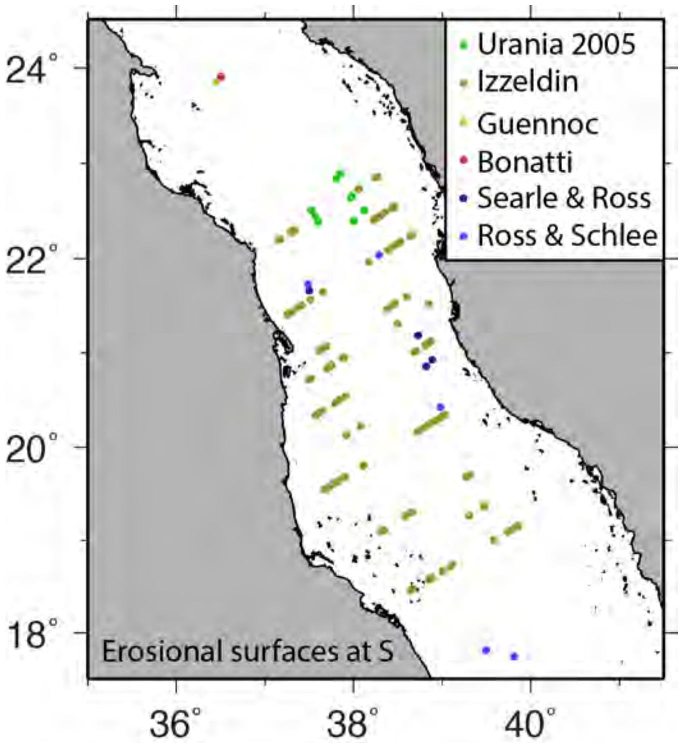

Figure 8. Central Red Sea occurrences of erosional surfaces at the top of the evaporites interpreted from truncated evaporite internal reflections in seismic data collected during the 2005 RV *Urania* cruise, the data of Izzeldin (1987), Guennoc et al. (1988) and Bonatti et al. (1984), and line drawing interpretations of Searle and Ross (1975) and Ross and Schlee (1973).

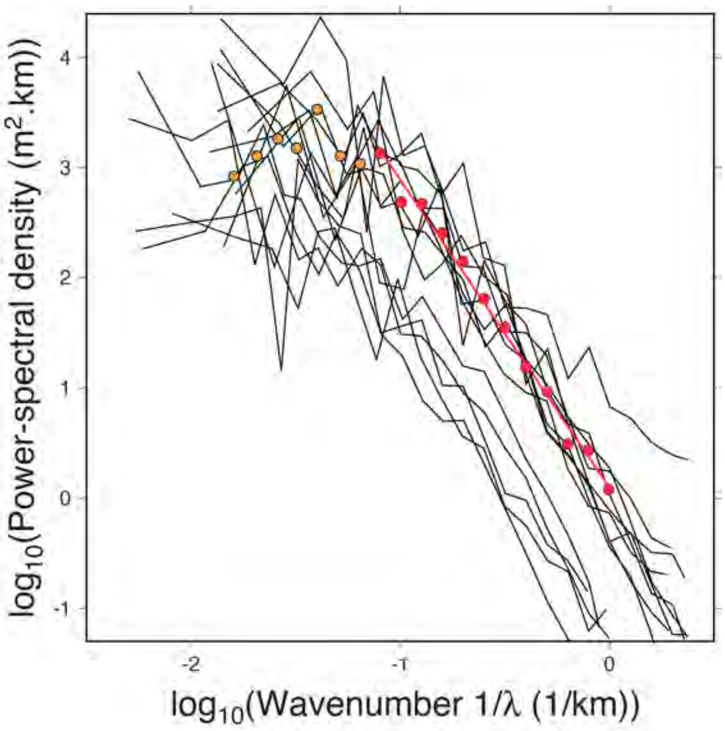

Figure 9. Power spectra of the selected lines of Figure 6. Power-spectral density was averaged within bins of 0.1 $\log_{10}$ units. Coloured circles represent averages of those spectra. Red line is a least-squares regression through the averages highlighted in red and has a graph gradient of -3.05.

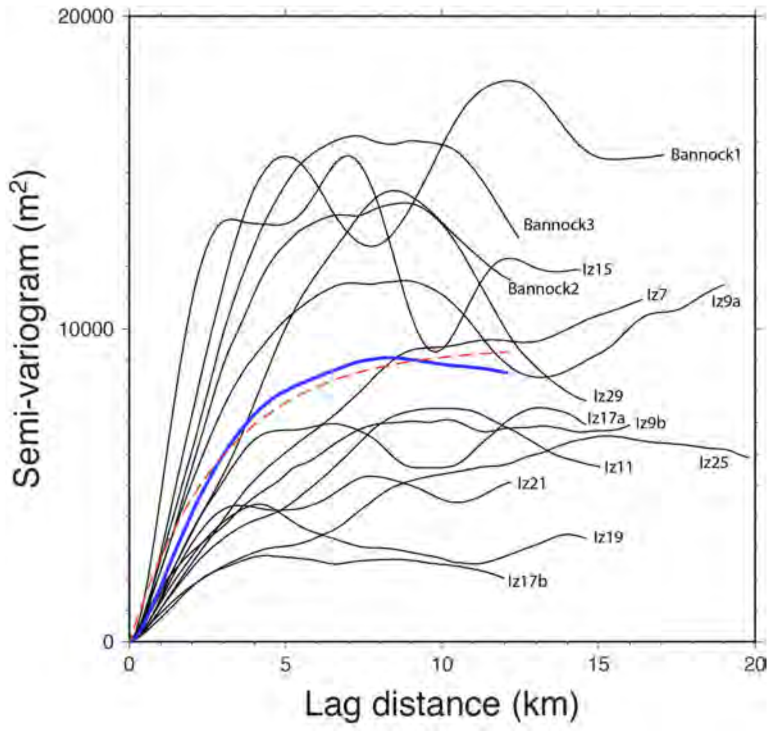

Figure 10. Variograms of the detrended S-reflection topography segmented as shown in Figure 6. Blue line is an average of the variograms shown. Dashed red line is an exponential model fitted to the average variogram by minimizing the squares of discrepancies ($\gamma(h)$ = 9428(1.0-exp(-h/3.0)) (m^2)).

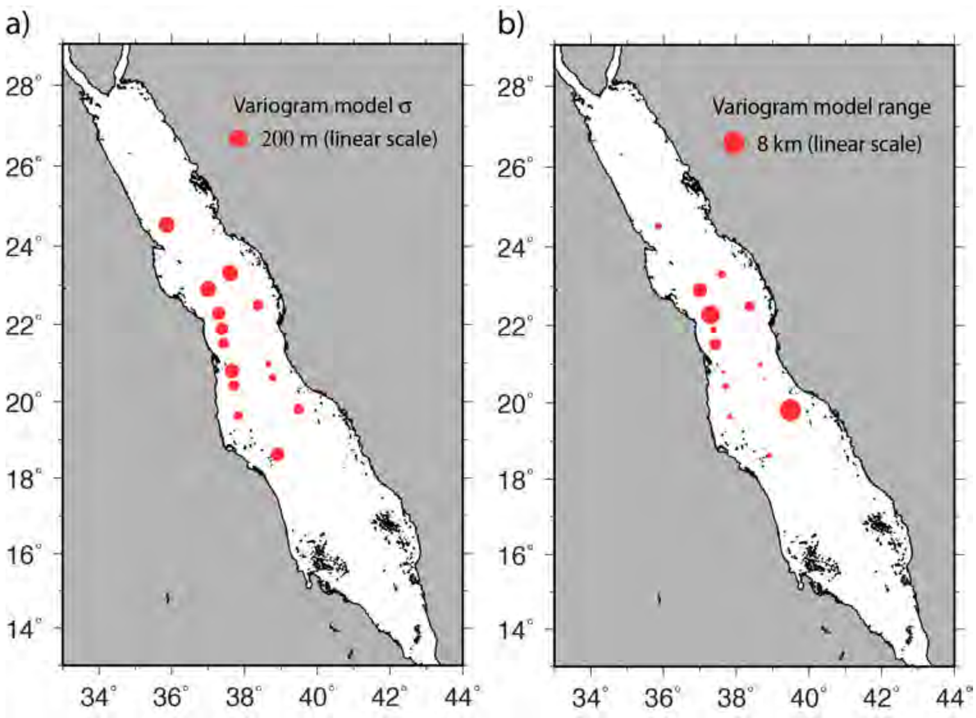

Figure 11. Maps of parameters of exponential models fitted to the variograms in Figure 10 by least squares: (a) Standard deviation σ (=√(2*c*)) and (b) range (*r* of equation (2)). Symbol diameters scale linearly with the variables shown.

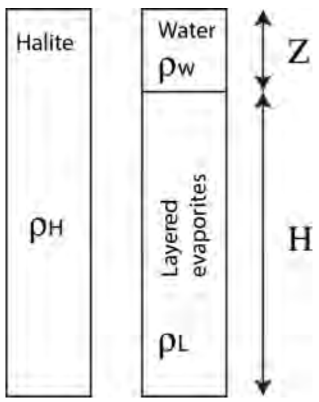

Figure 12. Simple isostatic model used to explore whether the excess topography *Z* over diapirs can reveal the depth extent *H* of layered evaporites between them using assumed densities for the components as shown.